The Astrophysical Journal, 795:159 (16pp), 2014 November 10 doi:10.1088/0004-637X/795/2/159

STRONG FAR-INFRARED COOLING LINES, PECULIAR CO KINEMATICS, AND POSSIBLE STAR-FORMATION SUPPRESSION IN HICKSON COMPACT GROUP 57

K. Alatalo[1,2], P. N. Appleton[1,2], U. Lisenfeld[3], T. Bitsakis[2,4], P. Guillard[5], V. Charmandaris[6,7,8], M. Cluver[9], M. A. Dopita[10,11,12], E. Freeland[13], T. Jarrett[9], L. J. Kewley[10], P. M. Ogle[1], J. Rasmussen[14,15], J. A. Rich[1,16], L. Verdes-Montenegro[17], C. K. Xu[1,2], and M. Yun[18]

[1] Infrared Processing & Analysis Center, California Institute of Technology, Pasadena, CA 91125, USA; kalatalo@ipac.caltech.edu
[2] NASA Herschel Science Center, IPAC, California Institute of Technology, Pasadena, CA 91125, USA
[3] Departamento de Física Teórica y del Cosmos, Universidad de Granada, E-18071 Granada, Spain
[4] Instituto de Astronomía, Universidad Nacional Autónoma de México, Aptdo. Postal 70-264, 04510 México, D.F., Mexico
[5] Institut d'Astrophysique Spatiale, Université Paris-Sud XI, F-91405 Orsay Cedex, France
[6] Institute for Astronomy, Astrophysics, Space Applications & Remote Sensing, National Observatory of Athens, GR-15236 Penteli, Greece
[7] Department of Physics, University of Crete, GR-71003 Heraklion, Greece
[8] Chercheur Associé, Observatoire de Paris, F-75014 Paris, France
[9] Astrophysics Cosmology and Gravity Centre, Dept of Astronomy, University of Cape Town, Private Bag X3, Rondebosch, 7701, Republic of South Africa
[10] Research School of Astronomy and Astrophysics, Australian National University, Cotter Road, Weston, ACT 2611, Australia
[11] Astronomy Department, King Abdulaziz University, P.O. Box 80203, Jeddah, Saudi Arabia
[12] Institute for Astronomy, University of Hawaii, 2680 Woodlawn Drive, Honolulu, HI 96822, USA
[13] The Oskar Klein Centre, Department of Astronomy, AlbaNova, Stockholm University, SE-106 91 Stockholm, Sweden
[14] Dark Cosmology Centre, Niels Bohr Institute, University of Copenhagen, Juliane Maries Vej 30, DK-2100 Copenhagen, Denmark
[15] Department of Physics, Technical University of Denmark, Building 309, DK-2800 Kgs. Lyngby, Denmark
[16] Observatories of the Carnegie Institution of Washington, 813 Santa Barbara Street, Pasadena, CA 91101, USA
[17] Departamento Astronomía Extragaláctica, Instituto Astrofísica Andalucía (CSIC), Glorieta de la Astronomía s/n, E-18008 Granada, Spain
[18] University of Massachusetts, Astronomy Department, Amherst, MA 01003, USA
Received 2014 May 27; accepted 2014 September 20; published 2014 October 28

ABSTRACT

We present [C II] and [O I] observations from *Herschel* and CO(1–0) maps from the Combined Array for Research in Millimeter Astronomy (CARMA) of the Hickson compact group HCG 57, focusing on the galaxies HCG 57a and HCG 57d. HCG 57a has been previously shown to contain enhanced quantities of warm molecular hydrogen consistent with shock or turbulent heating. Our observations show that HCG 57d has strong [C II] emission compared to $L_{\rm FIR}$ and weak CO(1–0), while in HCG 57a, both the [C II] and CO(1–0) are strong. HCG 57a lies at the upper end of the normal distribution of the [C II]/CO and [C II]/FIR ratios, and its far-infrared (FIR) cooling supports a low-density, warm, diffuse gas that falls close to the boundary of acceptable models of a photon-dominated region. However, the power radiated in the [C II] and warm H_2 emissions have similar magnitudes, as seen in other shock-dominated systems and predicted by recent models. We suggest that shock heating of the [C II] is a viable alternative to photoelectric heating in violently disturbed, diffuse gas. The existence of shocks is also consistent with the peculiar CO kinematics in the galaxy, indicating that highly noncircular motions are present. These kinematically disturbed CO regions also show evidence of suppressed star formation, falling a factor of 10–30 below normal galaxies on the Kennicutt–Schmidt relation. We suggest that the peculiar properties of both galaxies are consistent with a highly dissipative, off-center collisional encounter between HCG 57d and 57a, creating ring-like morphologies in both systems. Highly dissipative gas-on-gas collisions may be more common in dense groups because of the likelihood of repeated multiple encounters. The possibility of shock-induced star-formation suppression may explain why a subset of these HCG galaxies has been found previously to fall in the mid-infrared green valley.

Key words: galaxies: evolution – galaxies: individual (NGC 3753, NGC 3754) – galaxies: kinematics and dynamics – galaxies: star formation

Online-only material: color figures

1. INTRODUCTION

Hickson compact groups (HCGs; Hickson 1982) are small, relatively isolated systems of four or five galaxies in close proximity to one another. These high-density systems tend to have a high fraction of E/S0 galaxies compared with the field, show evidence of tidal interactions, and exhibit generally low group velocity dispersion (Hickson 1997). Verdes-Montenegro et al. (2001) studied the H I properties in HCGs and found that they were often H I deficient. Rasmussen et al. (2008) concluded that the H I deficiency could not be explained solely by the heating of the gas. Borthakur et al. (2010) were able to show that a non-negligible fraction of the missing H I might lie in an underlying diffuse component, but that diffuse component was unable to account for all missing H I. It was suggested that the level of H I depletion could be seen as part of an evolutionary picture for the groups, evolving from more H I-rich systems composed of mainly spiral galaxies toward groups with a higher fraction of elliptical and S0 galaxies (Konstantopoulos et al. 2010).

Johnson et al. (2007) investigated the infrared (IR) colors of HCGs, using the *Spitzer* IRAC diagnostic of Lacy et al. (2004). This work suggested that, unlike field galaxies, HCG galaxies seem to display a "gap" in the number of galaxies of intermediate IRAC colors, lying between dusty IRAC-red

galaxies and dust-free, stellar-dominated, IRAC-blue galaxies, roughly corresponding to late-type and early-type galaxies, respectively. This dearth in galaxies of intermediate color in HCGs led to the idea that the environment of HCGs might somehow accelerate the evolution from disks to early types (Tzanavaris et al. 2010; Walker et al. 2010, 2012, 2013). Bitsakis et al. (2010, 2011) studied the mid- and far-infrared properties of HCGs and found several trends in their specific star-formation rates and dust properties consistent with the idea that enhanced galaxy interactions in HCGs drive the evolution of the global properties of the groups.

Although the work of Bitsakis et al. (2010, 2011) shows that in larger HCG galaxy samples there is a small population of galaxies in the IRAC color "gap" region, they tend to be galaxies that lie in the UV–optical green valley even when their colors are corrected for optical extinction. Furthermore, these galaxies may have unusual dust properties when compared with galaxies in the field (Bitsakis et al. 2014).

The mid-IR spectroscopic capability of *Spitzer* opened up the ability to study the pure rotational lines of molecular hydrogen in a large sample of galaxies. In one system, Stephan's Quintet (also known as HCG 92), Appleton et al. (2006) and Cluver et al. (2010) discovered large quantities of intergalactic warm H_2 associated with a giant 40 kpc–scale shock in the system. Modeling of the observations suggests that strong turbulence was responsible for the formation of large quantities of warm H_2 from shocked H I gas (Guillard et al. 2009). The dissipation of turbulent energy is likely the main heating source of the molecular gas (Guillard et al. 2009, 2012a; Appleton et al. 2013). In a follow-up study, Cluver et al. (2013) studied 78 HCG galaxies in 23 groups and found that 20% showed unusually enhanced H_2 emission over and above that expected for heating by young stars alone ($I_{H_2}/I_{PAH(7.7\,\mu m)} \geqslant 0.04$). Such galaxies, termed molecular hydrogen emission galaxies (MOHEGs) by Ogle et al. (2007, 2010), are also common in samples of nearby radio galaxies, where the H_2 is also likely powered by shocks (Guillard et al. 2012b). When the HCG MOHEGs were placed on the IR color–color diagram, they were found to lie chiefly within the IRAC color "gap, leading Cluver et al. (2013) to postulate that shocks and turbulent heating might be connected to their "transitional" IRAC colors.

Observations with *Herschel* (Pilbratt et al. 2010) have allowed us to further investigate these transition objects in other excitation tracers, such as [C II] and [O I]. Although [C II] preferentially traces photon-dominated regions (PDRs) in diffuse gas and therefore correlates with star formation (the dominant energy source in most normal galaxies; de Looze et al. 2011), Appleton et al. (2013) have shown that in Stephan's Quintet, shocks are able to dominate the heating of the gas that gives rise to the [C II] emission. Given the likelihood that galaxy interactions are more common at higher redshifts, it is important to gauge the importance of shocks and turbulence in enhancing [C II] emission from galaxies.

It is also possible that the presence of shock-enhanced [C II] might be a signpost for *suppressed* star formation (SF). Ogle et al. (2010), Nesvadba et al. (2010), and P. Guillard et al. (2014, in preparation) show that in MOHEG radio galaxies, SF appears to be suppressed, possibly because of the turbulence induced by shocks as the radio jet traverses the molecular disk. Guillard et al. (2012a) and Konstantopoulos et al. (2014) conclude that SF is suppressed in the shock region of Stephan's Quintet. On the other hand, simulations (as well as observations of ULIRGs; Sanders & Mirabel 1996) seem to show that SF can be enhanced during a galaxy collision (Saitoh et al. 2009; Teyssier et al. 2010; Bournaud et al. 2011). The current simulations do not reach the dynamical range needed to probe both the large-scale injection of mechanical energy and the dissipation scale where low-velocity shocks or vortices dissipate the energy. This is why in simulations the role that shocks play in regulating star formation is not yet completely understood. Even stronger suppression of SF has recently been found in the early-type galaxy NGC 1266 (Alatalo et al. 2014), where suppression may be connected with an active galactic nucleus (AGN) outflow. Therefore, getting a census of the molecular gas, [C II] and other tracers of SF (such as the 24 μm dust emission; Calzetti et al. 2007) for a sample of likely shock-excited, early-type HCG galaxies may help us understand the connection between [C II] and SF in turbulent galaxies and provide insight into the potentially more turbulent era of high-z galaxies.

Here we present [C II] and [O I] maps from *Herschel* and CO(1–0) maps from the Combined Array for Research in Millimeter Astronomy (CARMA) for the inner part of HCG 57, which contains HCG 57a (=NGC 3753; a MOHEG) and its companions HCG 57d (=NGC 3754) and HCG 57c (=NGC 3750). Although this system is among the most H I deficient of the groups studied by Verdes-Montenegro et al. (2001), it contains copious quantities of warm molecular hydrogen. The rotationally excited H_2/PAH(7.7) ratio of HCG 57a is 0.17 (Cluver et al. 2013), which is the third highest of the entire HCG MOHEG sample, placing it clearly outside the range of H_2 excitation that can be explained by photoelectric heating alone. HCG 57a was also one of the few HCG galaxies observed by Cluver et al. (2013) to show significant extended warm H_2 along its major axis, with $M(H_2)_w = 1.8 \times 10^8\ M_\odot$ of warm ($T =$ 206 K) H_2 (over an area of 413 arcsecs^2, or 169 kpc^2). HCG 57c was not included as a target by the *Spitzer* Infrared Spectrograph (IRS) observations, and although there was some coverage of HCG 57d, there was no clear signal of warm H_2, and thus little is known about their warm H_2 properties. Both HCG 57a and d were detected with the Institut de Radioastronomie Millimétrique (IRAM) 30 m in CO(1–0) (Lisenfeld et al. 2014).

We intend to put forth HCG 57a and 57d as examples of the many ways that shocks and an interaction can influence the interstellar medium (ISM) and star formation within individual galaxies. We adopt a distance to HCG 57 of 132 Mpc, based on the luminosity distance of the most massive component, HCG 57a, and a Hubble constant of $H_0 = 67.3\,\mathrm{km\,s^{-1}\,Mpc^{-2}}$ and an updated ΛCDM cosmology with $\Omega = 0.315$, following the Planck parameters (Planck Collaboration et al. 2013). In Section 2, we describe the observations and data reduction from *Herschel* and CARMA of HCG 57a and HCG 57d. In Section 3, we compare the derived properties of each galaxy, including the spectra and fluxes of CO(1–0), [C II], and [O I]. In Section 4, we discuss the properties of each galaxy individually, compare those to normal galaxies, and build a picture of an encounter that might have created this system. In Section 5, we summarize our results.

2. OBSERVATIONS

2.1. Herschel

Herschel observations with the Photodetector Array Camera & Spectrometer (PACS; Poglitsch et al. 2010) were made on 2012 June 29 and 2012 July 5 of the inner HCG 57 group covering HCG 57a/c/d in a 3 × 3 mapping mode with a map step size of 38 arcsec. The observations were made as part

of a *Herschel* open-time program (OT2_appleto_2, PI: P. N. Appleton), and sparse mapping was performed over an area 123 × 123 arcsec^2. The spectrometer targeted the redshifted [C II] λ157.74 μm and [O I] λ63.18 μm lines, providing effectively 1408 s and 2464 s of integration time at each of the nine pointings. Two "range-mode"grating scans were obtained, covering a larger radial velocity range for the group (2600 km s^{-1} for [C II] and 1990 km s^{-1} at [O I]) than a standard spectral-line observation. The "chop-nod" mode was used with a (large) chopper-throw of 3 arcmin, which ensured that the "off" position at each chopper position was clear of any galaxies.

The PACS data reduction was performed using the Herschel Interactive Processing Environment (HIPE) software package CIB13-3069 made available by the PACS team for our project. Data processing was performed on the level-0 data (raw data) via the interactive pipeline and included flagging (and ignoring) of bad pixels and saturated data, subtraction of chop "on" and "off" data, division of the relative spectral response function (RSRF), and the application of a flat field. These data were converted from standard data frames to rebinned data cubes by binning these data in the wavelength domain using default parameters (oversample = 2, upsample = 4), which sample the spectra at the Nyquist rate in the two bands. Finally, data for the two nods were averaged, and final data cubes were created with 3 × 3 arcsec^2 projected pixels on the sky using a new projection algorithm called "specInterpolate. This new algorithm, which we obtained in advance of the full release of HIPE 13, will become the projection algorithm recommended by the PACS team for this kind of PACS spectral mapping. Unlike previous projection methods (e.g., specProject), which simply divides up and averages flux from the PACS spectrometer spaxel measurement (9.4 × 9.4 arcsec^2) onto the sky in a simplistic way, the new algorithm uses a triangulation interpolation algorithm to more correctly distribute and average the various individual integral field unit pointings onto sky coordinates. We have extensively tested the algorithm for flux conservations with many different data sets and confirm that the new and older (specProject) algorithms conserve flux equally well. We assume that the absolute flux calibrations for the red [C II] and blue [O I] final data cubes are uncertain by 12% and 11%, respectively, based on calibration observations of standard calibrators.

Once channel maps of the *Herschel* [C II] and [O I] were created, the moment maps were constructed in Interactive Data Language (IDL). The data cubes were Gaussian smoothed spatially (with a FWHM equal to that of the *Herschel* point-spread function (PSF) at 160 μm of 9.4 arcsec), and masks were created by selecting all pixels above fixed flux thresholds, adjusted to recover as much flux as possible in the moment maps while minimizing the noise (generally about two to three times the rms noise in the smoothed channels). The moment maps were then created using the spatially unsmoothed cubes within the masked regions and integrating over the channel range where the mask indicated emission was detected. The *Herschel* PACS spectral resolution for [C II] was 230 km s^{-1} and had a spectral step of 29.8 km s^{-1}. The [O I] maps were obtained with higher spectral resolution (90 km s^{-1}) with a spectral step of 10.4 km s^{-1}.

2.2. CARMA

Observations were carried out at the CARMA observatory between 2013 March 12 and 2013 March 17 in the D configuration (corresponding to baselines of 11–150 m, resolving scales between 3.6 and 48 arcsec at CO(1–0). Observations included a long integration on a bright quasar (in this case, 3C273) in order to calibrate the passband response of the telescopes. Observations were then taken in a repeating sequence, alternating between HCG 57a for 16 minutes and a phase calibrator (the quasar 1224+213) for 2 minutes. HCG 57a was observed for a total of 7.37 hr. HCG 57d was within the primary beam of the HCG 57a field. HCG 57c was also within the primary beam of the 6 m CARMA antennas, but it was undetected in CO(1–0).

Raw CARMA data were reduced using the Multichannel Image Reconstruction Image Analysis and Display (MIRIAD) package (Sault et al. 1995), with the method of reduction and analysis identical to what is described in Section 3.2 of Alatalo et al. (2013), and had a synthesized beam of 4.6 × 3.″3. Data cubes were constructed with 30 km s^{-1} channels of the central 90″, corresponding to the FWHM of the primary beam of the 6 m antennas. Moment maps were then constructed using MIRIAD, following the same method as described in Alatalo et al. (2013).

3. RESULTS AND ANALYSIS

Figure 1 shows the [C II] and CO(1–0) integrated distribution and mean kinematics, overlaid on both the infrared and the optical light. Only the large edge-on disk galaxy (HCG 57a) and the small ring galaxy (HCG 57d; visible in *Spitzer* IRAC imaging) are detected by Herschel and CARMA; the elliptical galaxy HCG 57c is not detected. The warp in the disk of HCG 57a suggests that it has been in a gravitational interaction, most likely with HCG 57d. The two-dimensional separation between the nuclei of HCG 57a and HCG 57d is 22″, or 13 kpc on the sky, and the difference in the systemic velocities is 250 km s^{-1}. The CO(1–0) and [C II] velocity fields are consistent with one another, given the difference in spatial resolution between the two instruments and some contamination of the [C II] velocity field of HCG 57a by HCG 57d. The largest mixing of kinematic components occurs in the southeastern part of the disk, where the channel maps show the largest overlap of emission between the two galaxies. Bearing in mind this effect, the channel maps suggest that the CO and [C II] represent relatively well-mixed kinematic components. A good example is the kinematics of HCG 57d, which in both [C II] and CO(1–0) shows a gradient in the direction of HCG 57a, supporting the idea that this galaxy is interacting with the larger galaxy. It is also possible that the [C II] channel maps in Figure 2 show a [C II] bridge between the galaxies, but the resolution and spaxel size of *Herschel* PACS are such that we cannot rule out a simple superposition of gas from the two galaxies in that region.

Emission from the [O I] λ63 μm line was faintly detected from HCG 57d (and not at all from HCG 57a). Unlike the emission from [C II], Figure 3 shows that the [O I] is more concentrated along the eastern edge of the galaxy in the region where the ring is especially prominent in near-IR observations. The [O I] emission is not detected in HGC 57a.

The integrated distributions of [C II] and CO(1–0) show large differences between the two galaxies. HCG 57d, the dominant [C II] and [O I] emitter in the system, is quite weak in CO(1–0), whereas the opposite is true for HCG 57a. To further explore this effect, we present the [C II] and CO(1–0) channel maps in Figures 2 and 4. The [C II] channel maps (Figure 2) were overlaid on the *Spitzer* 8 μm nonstellar emission.[19] The channel maps

[19] This image was obtained by convolving the 3.6 μm image to the resolution of the 8 μm observations, and then subtracting it from the 8.0 μm image with a scaling factor of 0.232 (Helou et al. 2004). This map is therefore dominated by polycyclic aromatic hydrocarbon (PAH) emission and warm dust (if present).

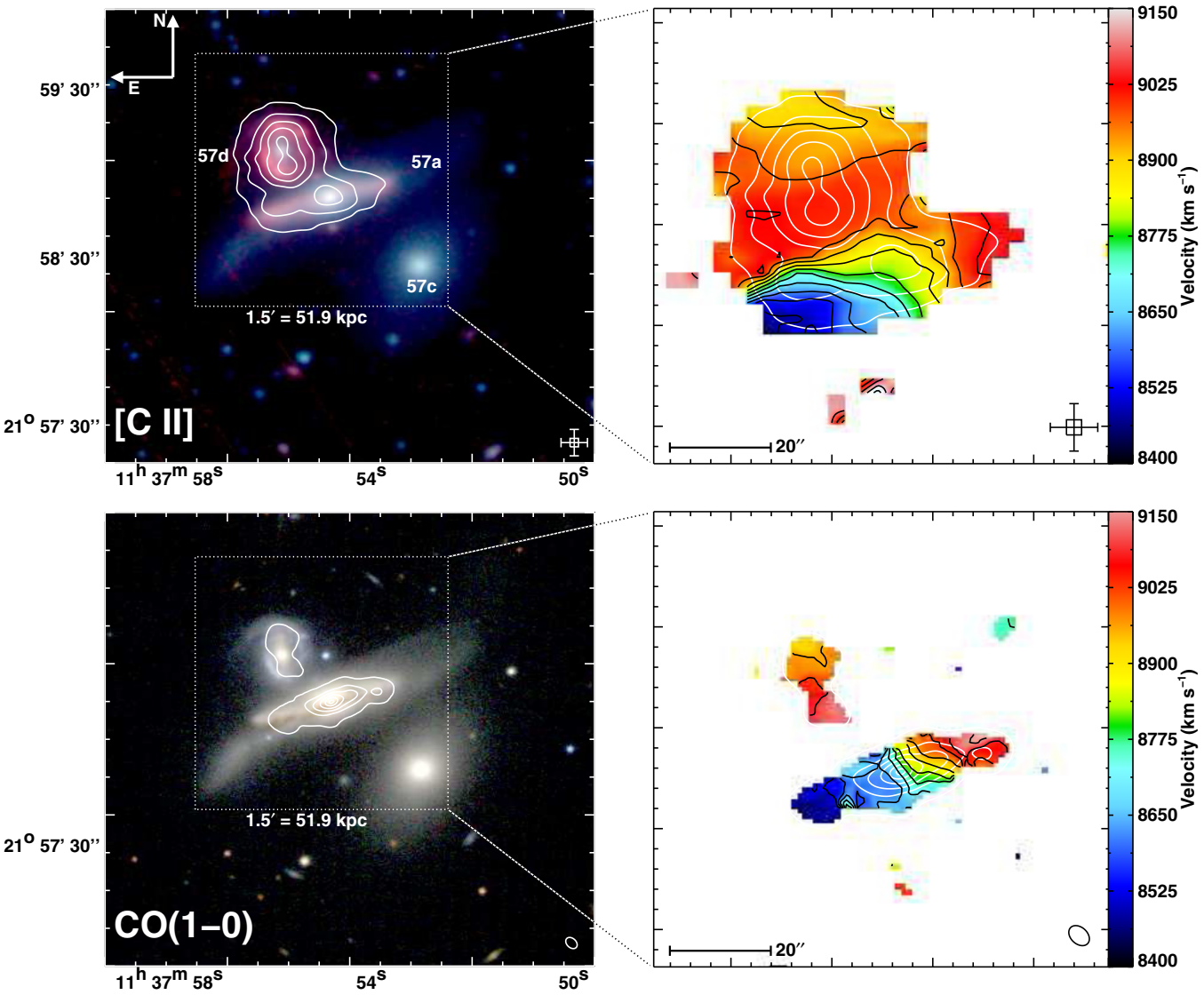

Figure 1. Top: the *Spitzer* 3.6 μm−4.5 μm−8.0 μm true color image (left, corresponding to blue, green, and red, respectively) is overlaid with the integrated intensity contours (moment 0; white) of the *Herschel* [C II] emission detected in HCG 57. The dotted line box represents an area that is 1.′5 on a side. A zoomed-in map is shown on the right that includes the mean velocity (moment 1) map of the [C II] data from *Herschel*, overlaid with isovelocity contours (black) as well as the moment-0 contours (white). Bottom: the three-color *g*-*r*-*i* SDSS image (left) is overlaid with the CO(1–0) moment-0 map from CARMA (white contours). A zoomed-in map is shown on the right that includes the moment-1 map of the CO(1–0) overlaid with isovelocity contours as well as moment-0 contours. Major tick marks on both three-color images represent 1′ and 20″ on each moment-1 map. The CO(1–0) and [C II] velocity fields are consistent with one another, given the difference in spatial resolution between the two instruments and some contamination of the [C II] velocity field of HCG 57a by 57d. The largest mixing of kinematic components occurs in the southeastern part of the disk where the channel maps show the largest overlap of emission between the two galaxies.

(A color version of this figure is available in the online journal.)

confirm that [C II] is found throughout the disk of HCG 57a, but it is brightest in HCG 57d. The CO(1–0) channels from CARMA are overplotted on the three-color Sloan Digital Sky Survey (SDSS) image of HCG 57 (Figure 4). It is clear that there is much stronger CO emission in HCG 57a than in HCG 57d, although weak (signal-to-noise ratio (S/N) per channel ≈3) emission is detected in HCG 57d, with a strong north–south velocity gradient as discussed earlier.

Lisenfeld et al. (2014) observed HCG 57a and 57d with the IRAM 30 m. Our CARMA observations recover 87% of the IRAM 30 m flux for HCG 57a and 51% for 57d. The 87% flux recovery in HCG 57a is well within calibration errors for millimeter observations. Table 1 lists the velocity bandwidth and fitting parameters used for each system, and Table 2 shows the derived fluxes. In HCG 57d, the underrecovery by

Table 1
Flux Fitting Parameters for HCG 57

HCG 57d	CO(1–0)	[C II]	[O I]
v_{cen} (km s^{-1}) =	8976 ± 13	8977 ± 4	9000 ± 28
FWHM (km s^{-1}) =	212 ± 30	309 ± 9	204 ± 67
Peak Flux Density (Jy) =	0.02 ± 0.003	12.0 ± 0.31	1.6 ± 0.5
HCG 57a	Region 1	Region 2	Region 3
CO(1–0) Bandwidth (km s^{-1})			
8230–9342	8388–9023	8230–9183	8547–9278
[C II] Bandwidth (km s^{-1})			
7910–9523	7910–9284	8120–9404	8537–9524
[O I] Bandwidth (km s^{-1})			
8306–9351 for all regions			

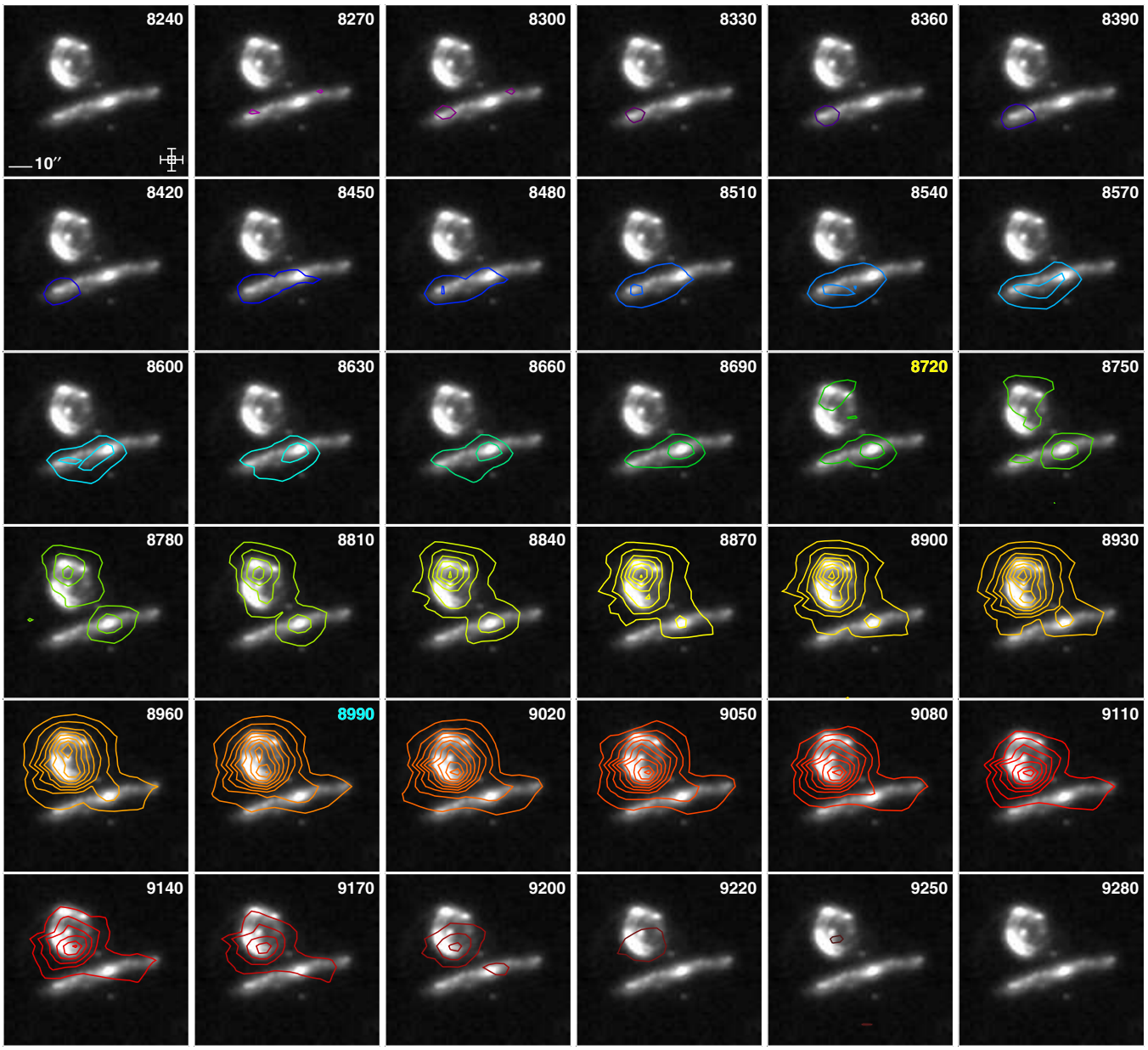

Figure 2. [C II] channel maps from *Herschel* listed in heliocentric, optically defined velocities, with contour colors presented relative to the systemic velocity of HCG 57a overlaid on the *Spitzer* continuum-subtracted nonstellar 8.0 μm image. The [C II] contour colors represent the red- and blue-shifted components seen. Contours begin at the $\pm 3\sigma$ level and then are made in 3σ increments, with gray contours representing negative contours. In the first panel, we show a size scale (bottom left), and the 9.″4 Herschel PACS native spaxel is shown as a cross, overlaid with the chosen pixel size (3″) for the combined, projected [C II] maps (bottom right). [C II] is brightest in HCG 57d, but fainter emission is clearly present over a wide range of velocities in HCG 57A, especially near the nucleus. Velocity labels with channels closest to the systemic velocities of HCG 57a (of 8727 km s^{-1}) and of HCG 57d (of 8977 km s^{-1}) are displayed in yellow and cyan, respectively. The color of the contours consistently represents a velocity range between 8240 and 9330 km s^{-1}.

(A color version of this figure is available in the online journal.)

the interferometer of flux could possibly be due to a large underlying mass of diffuse CO emission; however, the overall faintness of CO in HCG 57d means that we are signal-to-noise limited on the scale of the synthesized beam of the interferometer for this galaxy. Therefore, for the purposes of the *global* properties of HCG 57d, we assume the 30 m measured CO fluxes, luminosities, and masses. When deriving properties such as star-formation surface density (Section 4.3), because the area of the emitting source is important, we use the CARMA-derived areas and surface densities for HCG 57d.

In order to create data cubes suitable for spectral comparisons, we convolved the CO(1–0) map to the resolution of the [C II] data (9.″4). The smoothed data cube was then used to make moment maps using `MIRIAD` as described in Alatalo et al. (2013). The resultant CO(1–0) maps were then registered to the same coordinate system as the [C II] map. The [O I] emission was only detected in HCG 57d. The [O I] data cube was registered to the coordinate system of the [C II] map, but was not convolved because the only emission detected (associated with HCG 57d) is quite compact and well contained within the large extraction region centered on that region. Spectra (described in the next subsections) were then extracted in four chosen regions: one centered on HCG 57d and three regions covering HCG 57a. All [C II] and [O I] pixels from the registered cubes lying inside

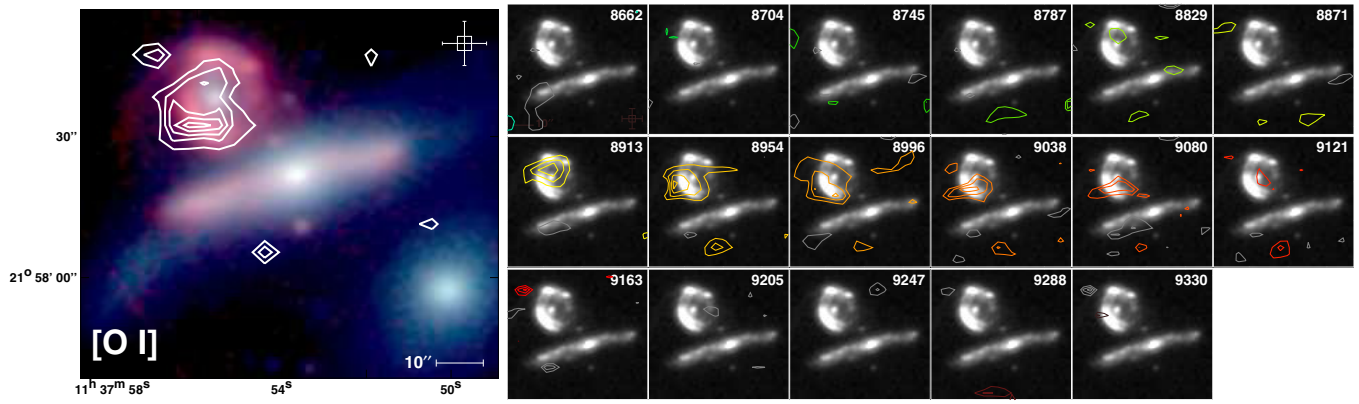

Figure 3. Left: the *Spitzer* 3.6 μm−4.5 μm−8.0 μm true color image (left, corresponding to blue, green, and red, respectively) is overlaid with the integrated intensity contours (moment 0; white) of the *Herschel* [O I] emission detected in HCG 57, showing that [O I] is primarily detected in HCG 57d. Right: the *Spitzer* continuum-subtracted nonstellar 8.0 μm image is shown with the individual [O I] channel maps from *Herschel* listed in heliocentric, optically defined velocities, with contour colors presented relative to the systemic velocity of HCG 57a. The colors of the contours represent the red- and blue-shifted components seen. Contours begin at the $\pm 2\sigma$ level and then are made in 1σ increments, with gray contours representing negative contours. In the first panel and moment map we show a size scale (bottom left), and the 9.″4 Herschel PACS native spaxel is shown as a cross overlaid with the chosen pixel size (3″) for the combined, projected [O I] maps (bottom right). The [O I] emission mainly follows the eastern side of the ring in HCG 57d, especially at higher systemic velocities. The color of the contours consistently represents a velocity range between 8240 and 9330 km s^{-1}.

(A color version of this figure is available in the online journal.)

Table 2
HCG 57 [C II], CO(1–0), and [O I] Luminosities[a]

	$L_{[C\,II]}$ $10^7\times(L_\odot)$	$L_{CO(1-0)}$ $10^4\times(L_\odot)$	$L_{[O\,I]}$ $10^6\times(L_\odot)$	L_{TIR}[b] $10^9\times(L_\odot)$	L_{FIR}[b] $10^9\times(L_\odot)$	[C II]/L_{FIR} $\times10^{-3}$	CO(1–0)/L_{FIR} $\times10^{-6}$	[C II]/[O I]	[C II]/CO(1–0)
HCG 57d	12.5 ± 0.51	2.05 ± 0.22[c]	27.4 ± 12.	21.1 ± 5.6	8.4 ± 2.3	15. ± 4.1	2.4 ± 0.7	4.6 ± 2.	6100 ± 690
HCG 57a	7.99 ± 0.18[d]	9.95 ± 0.49	<13.2	23.3 ± 4.2	6.24 ± 1.2	13. ± 2.	16. ± 3.1	>6.1	804. ± 43.
Region 1	2.47 ± 0.14[d]	1.83 ± 0.24	<8.6	8.65 ± 2.8	2.5 ± 0.87	9.8 ± 3.5	7.3 ± 3.	>2.9	1350 ± 190
Region 2	2.48 ± 0.09	5.49 ± 0.22	<5.0	7.9 ± 2.0	1.7 ± 0.5	14. ± 4.4	31.6 ± 9.9	>5.0	452. ± 25.
Region 3	2.17 ± 0.09	2.45 ± 0.17	<7.3	6.7 ± 1.9	2.0 ± 0.6	11. ± 3.2	12. ± 3.6	>3.0	887. ± 73.

Notes.
[a] Assuming a luminosity distance $D = 132$ Mpc.
[b] L_{FIR} is 42.5–122.5 μm (Helou et al. 1988) and L_{TIR} is from 8–1000 μm, values from Bitsakis et al. (2014).
[c] From Lisenfeld et al. (2014), $L_{CO} = 1.07 \pm 0.22 \times 10^4\ L_\odot$ recovered from CARMA.
[d] Includes a correction for [C II] contamination from HCG 57d of 9% for the total HCG 57a system and 32% for Region 1, 15% for Region 2, and no contamination for Region 3.

the extraction regions of Figure 5 were summed to create the spectra. An additional step was taken for the [C II] spectrum in Region 1 of HCG 57a, which likely included a contribution from the background HCG 57d. Figure 6(b) indicates that there is a large redshifted [C II] peak that is not also traced by CO(1–0) emission, which is the component suspected of being part of the contamination.

A two-Gaussian fit was run on the Region 1 [C II] spectrum, and gas that appeared centered on v_{sys} of HCG 57d was measured to be ≈40% of the total [C II] signal from Region 1. The boundaries of Region 2 were chosen specifically to minimize [C II] contamination of HCG 57a from HCG 57d by careful inspection of the [C II] data cube. By extracting spectra from between the two galaxies and estimating the extent of the emission "skirt" from HCG 57d in the relevant velocity channels toward HCG 57a, we believe the contamination of Region 2 is between 10% and 15% over its broad [C II] velocity profile. This relatively low total contamination is aided by the fact that the centroid of the main [C II] emission from HCG 57d shifts to the southeast at velocities around 9,000 km s^{-1} and higher, largely avoiding Region 2. Furthermore, emission isolated to the central regions of HCG 57a is observable in a wide range of channels, even over the range where the two galaxies have similar velocities, again suggesting that the contamination is not large. Strong contamination would pull the observed emission centroid away from the center of HCG 57a, which is not observed except perhaps in the channels between that are centered on 8960 and 8990 km s^{-1}. Region 3 does not appear to suffer significant contamination. The total [C II] luminosities for the galaxies and selected regions throughout this paper take these estimated contamination factors into account.

Due to the low S/N nature of the CO(1–0) cube, an extra step was added to CO spectral extractions. The pixels with nonzero emission in the smoothed CO(1–0) moment-0 map inside the region were the only ones considered in making the spectrum. This avoided adding large, noise-dominated areas to the integral, which would dilute the CO(1–0) signal. The right panels in Figure 5 identify the extractions that were used in making the spectra of [C II] and CO(1–0) for each region.

3.1. HCG 57d

The CO(1–0) distribution and kinematics within HCG 57d appear to represent emissions originating from the northern and southern parts of a face-on ring (which is most obvious in the nonstellar 8 μm emission seen in the top left panel of Figure 2). The CO(1–0) kinematics (seen in Figures 1(b) and 4)

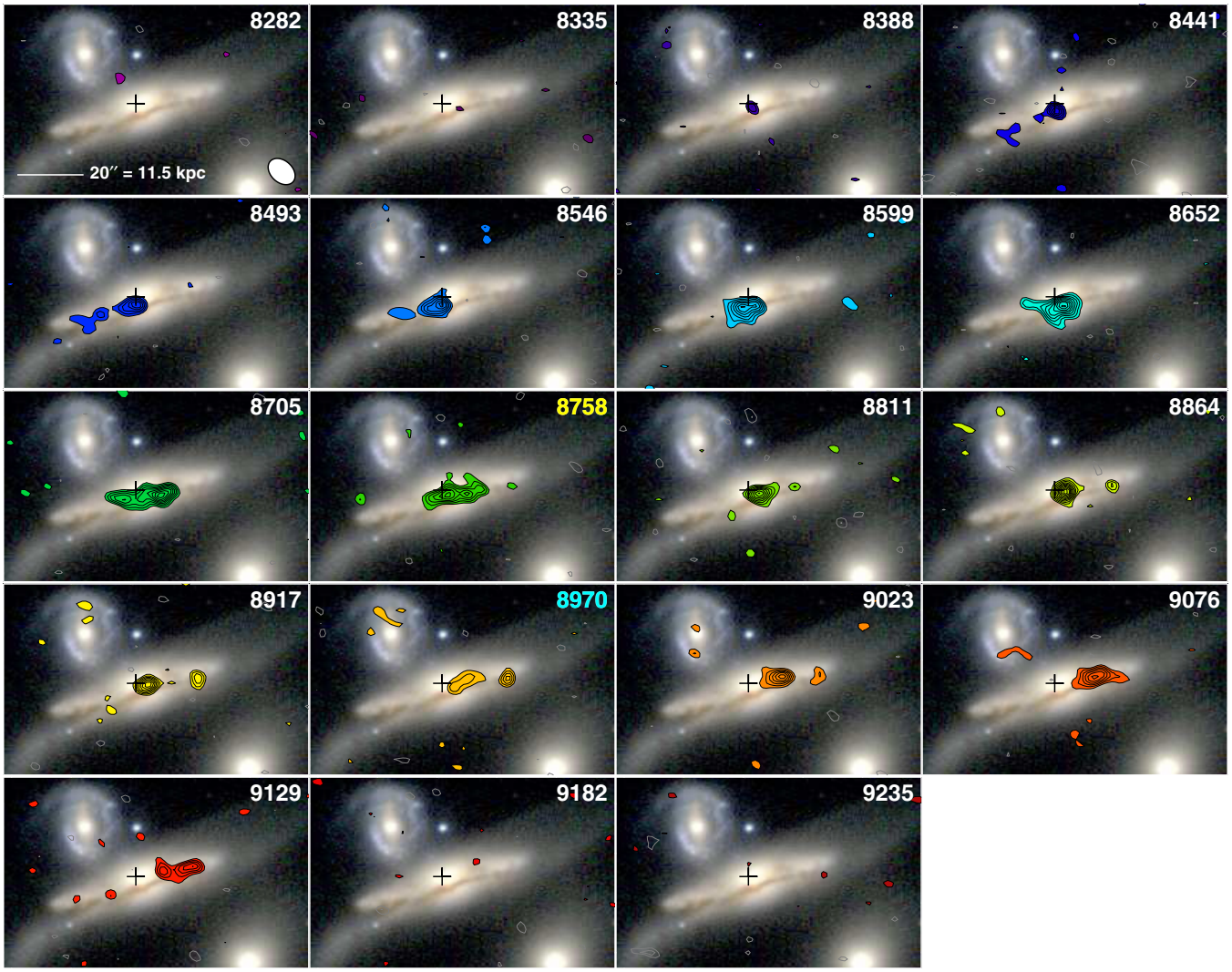

Figure 4. *g-r-i* SDSS image shown with the individual CO(1–0) channel maps from CARMA, listed in heliocentric, optically defined velocities with contour colors relative to the systemic velocity of HCG 57a. The colors of the contours represent the red- and blue-shifted components seen. The black cross in each panel represents the nucleus of HCG 57a determined from the 2MASS imaging. Contours begin at the $\pm 2.5\sigma$ level and then are made in 1σ increments, with gray contours representing negative contours. A size scale as well as the synthesized beam size of CARMA of 4.6 × 3.3 arcsec are shown in the first panel. Channels closest to the systemic velocities of HCG 57a (of 8727 km s^{-1}) and of HCG 57d (of 8977 km s^{-1}) are listed in yellow and cyan, respectively. The color of the contours consistently represents a velocity range between 8240 and 9330 km s^{-1}.

(A color version of this figure is available in the online journal.)

in HCG 57d also appear fairly regular and in general follow the kinematics of the brighter (but also less well resolved) [C II] emission. As discussed previously, the [O I] emission seems to follow the eastern and southeastern segment of the star-forming ring, as seen in 3.

The integrated CO(1–0), [C II], and [O I] spectra for HCG 57d are shown in Figure 7. The spectra are quite similar, suggesting that the atomic gas and molecular gas are well mixed, although the [O I] have a slightly higher systemic velocity than the [C II] and CO, perhaps because it has a slightly different distribution from the [C II]. In order to derive the integrated line fluxes, each line was fit by a single Gaussian profile using the IDL code `gfitflex`.[20] Table 1 presents the fitting parameters for the Gaussian fits for CO(1–0), [C II], and [O I] for HCG 57d. Table 2 presents the results and their total errors.[21] The [C II]/CO(1–0) ratio is ≈6100 larger than is seen in most galaxies (≈1000; Malhotra et al. 2001), although it is consistent with the extreme starburst from Stacey et al. (1991) and the high-z galaxies from Stacey et al. (2010; with a [C II]/CO(1–0) average of ∼6000). The extreme environments of the starbursts and submillimeter galaxies support extremely large ultraviolet fields (log $G_0 > 3$), which is inconsistent with the observations of HCG 57d, discussed in more detail in Section 4.1.

3.2. HCG 57a

Figure 8 shows the [C II] and CO(1–0) position-velocity diagram (PVD) of HCG 57a of a slice intersecting the disk (shown in the inset panel). The [C II] emission and the CO(1–0) emission seem to have broadly similar distributions, but the [C II] PVD contains some contamination from HCG 57d around 9000 km s^{-1} because of the generous width chosen for the extraction box. The CO(1–0) map suffers less contamination because of the smaller beam. In the CO(1–0), instead of a single velocity component, HCG 57a seems to have three.

[20] http://astro.berkeley.edu/∼heiles/handouts/handouts_idl.html
[21] A sum of the fitting errors and the rms noise in the individual pixels.

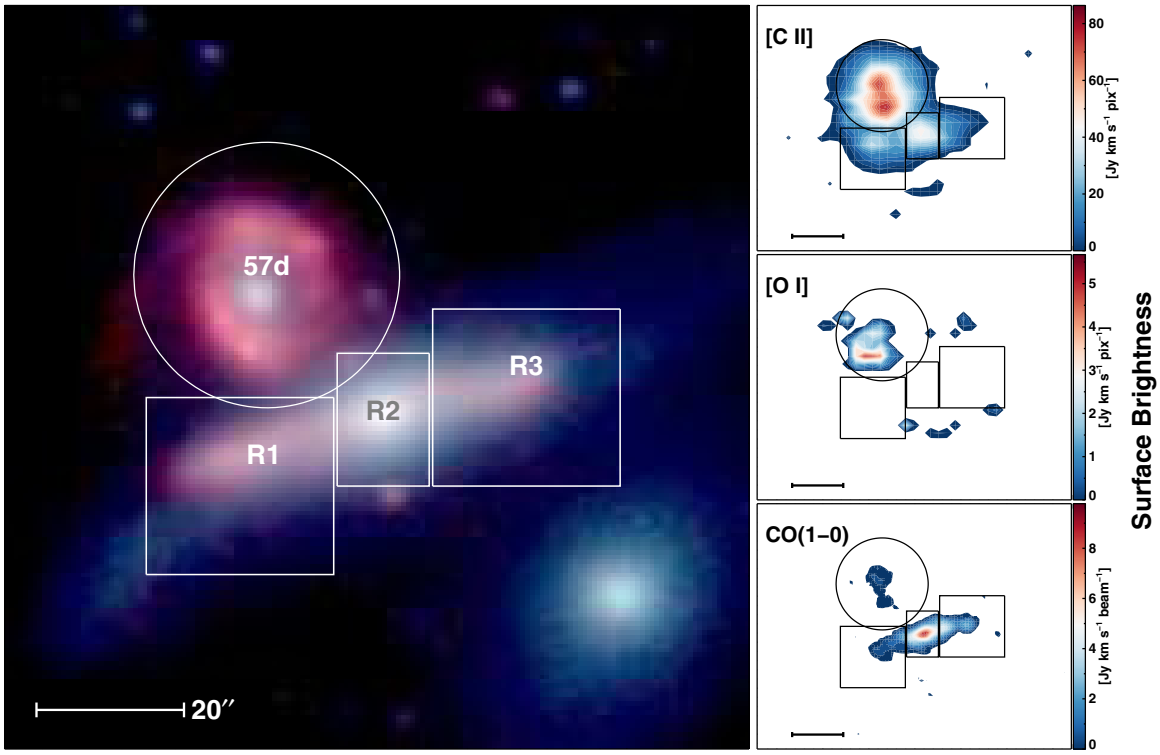

Figure 5. Three-color *Spitzer* IRAC 3.6, 4.5, 8.0 μm true color image (left) shows the demarcated regions on HCG 57a as well as the circular region used to extract spectra for HCG 57d. (Right) The smoothed integrated intensity maps in units of surface brightness of [C II], [O I], and CO(1–0) are also shown with the regions overlaid.

(A color version of this figure is available in the online journal.)

First, there is a regularly rotating component, seen as an S-shaped curve that begins in the lower left of the PVD in Figure 8 and terminates in the upper right, shown in white on the schematic. This component extends throughout the CO extent.

The second kinematic component in the PVD is seen at the top right, but it has a smaller velocity extent, deemed the splash ring. The splash ring seems to be a tight knot of molecular gas, seen in the velocity slices from 31–349 km s^{-1} (8758–9076 km s^{-1}) in the CO channel map shown in Figure 4 on the right-hand side of the main velocity component within the HCG 57a disk. The knot also appears to be correlated with extinction, which is visible in the underlying SDSS three-color image.

The third kinematic component spans a small spatial scale and a large velocity, ranging from −400 to +250 km s^{-1} (8277 to 8977 km s^{-1}), labeled the compact, high-velocity component. This broad component is offset from the peak of the CO(1–0) magnitude, which corresponds to the nucleus of the galaxy. This kinematically broad and spatially compact kinematic component lacks the symmetry expected from a bar, which would be corotating with the disk. It is therefore possible that this broad, compact kinematic component is either an inflow or an outflow. While ±325 km s^{-1} is large, this component does not exceed the escape velocity. Lisenfeld et al. (2014) shows that the broad CO velocities in HCG 57a compared with $L_{K\,2.2\,\mu\mathrm{m}}$ of the galaxy make it an outlier compared with the other MOHEGs. The high-velocity feature is offset from the nucleus (measured using a 2MASS image; Skrutskie et al. 2006) by ≈4″, meaning it is less likely to be an AGN-driven outflow and may be tidal in origin.[22]

[22] We note that HCG 57a shows only weak evidence of an active nucleus, having a marginally enhanced [N II]/Hα optical emission line ratio (Martínez et al. 2010).

Torres-Flores et al. (2014) claim the detection of a faint Hα structure connecting HCG 57d to the center of HCG 57a, and it is possible that the compact, high-velocity component might be related. The separation of these distinct CO components is not currently possible within the [C II] because of the limitations of the spatial (9.″4) resolution of *Herschel*. It is also possible that there is a faint, diffuse CO emission associated with [C II] from HCG 57d, but it falls far below the detection threshold of CARMA and can be considered negligible.

Following the kinematic components of the PVD, HCG 57a was divided into three separate regions when constructing integrated CO(1–0) and [C II] line profiles, using the region boxes labeled on Figure 5. Each region is dominated by a different molecular kinematic component. Region 1 (R1), at the lower left corner of HCG 57a, appears to only have the regular rotation component in the CO(1–0) PVD. Region 2 (R2) encompasses the nuclear region of HCG 57a, which includes the compact, high-velocity kinematic feature and regular rotation, and R3 is found at the top right, which includes the regular rotation component and the splash ring component in the northwest region of the PVD.

The boundaries of R2 were chosen from a careful exploration of the emission in the PACS data cube to minimize obvious contamination of emission in [C II] from HCG 57d. Figure 6 presents the [C II] and CO(1–0) spectra for each region and an integrated spectrum of all regions. The total luminosities for all regions were calculated by summing all channels inside the shaded velocity ranges (blue for CO(1–0) and yellow for [C II]) on the plots in Figure 6. Because of the complex structure of both [C II] and CO(1–0), summing over all channels with emission was preferable to attempting to fit the spectra with Gaussian profiles. Table 2 presents the [C II] and CO(1–0) line

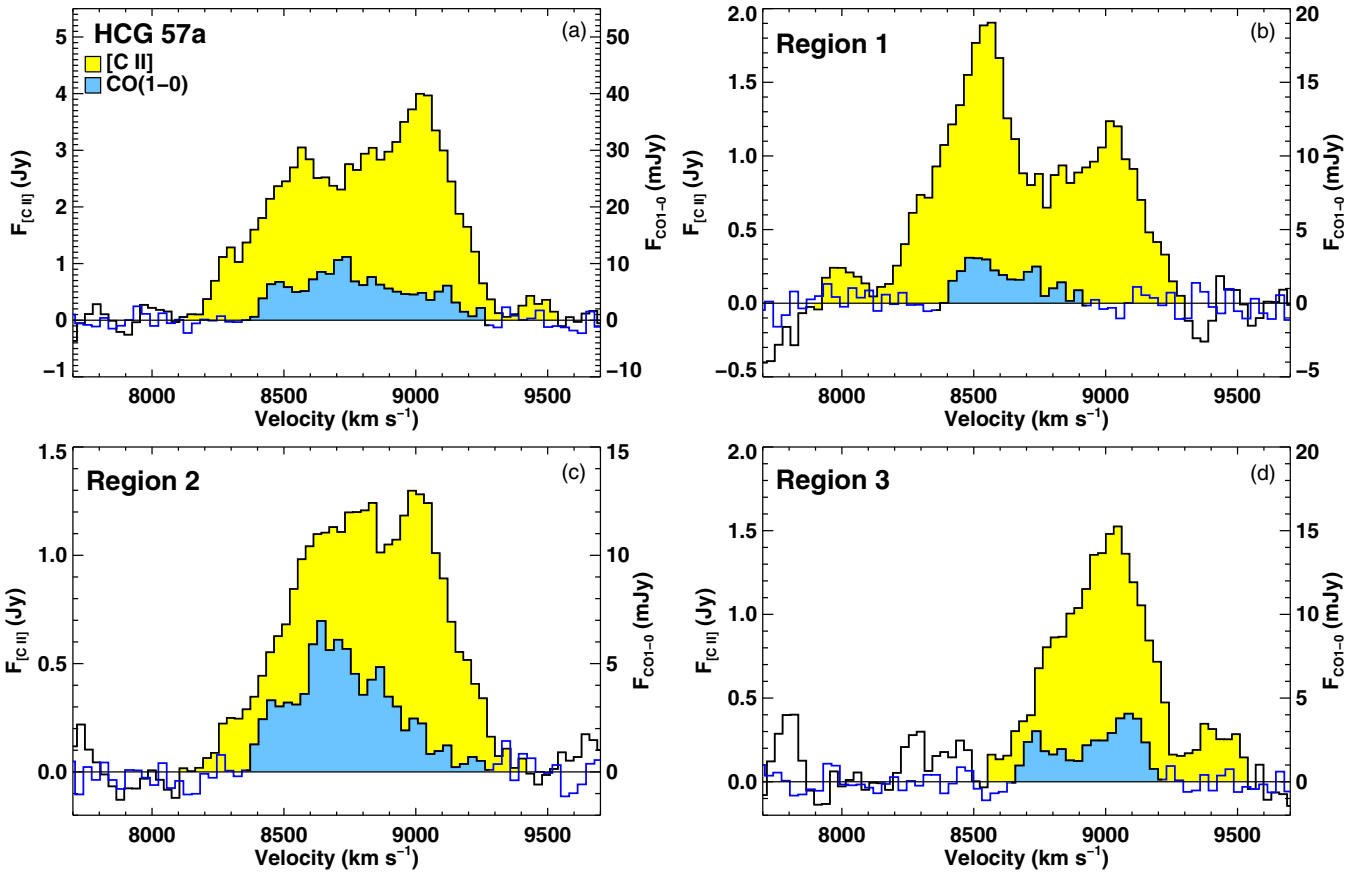

Figure 6. *Herschel* [C II] emission (yellow) compared to the CO(1–0) emission from CARMA (blue) in HCG 57a as well as the three subregions. In most cases, the [C II] and CO(1–0) appear to trace gas of a similar velocity, except in the case of Region 1, in which the [C II] flux arising at $v \approx 9000$ km s^{-1} is likely contamination from HCG 57d. We estimate that less than 15% of the [C II] emission from Region 2 is contamination from HCG 57d (see text).

(A color version of this figure is available in the online journal.)

luminosities of the regions of HCG 57a. The [C II]/CO(1–0) ratio varies from region to region, ranging between 560 and 1380. Unlike in the case of HCG 57d, these ratios do not fall outside the range for normal galaxies (Stacey et al. 2010).

4. DISCUSSION

The HCG 57 system was targeted by our team using *Herschel* to try to gain more understanding of systems with high, warm H_2/PAH ratios as derived from *Spitzer*, which are surmised to be shock-dominated systems. In particular, the disk of HCG 57a was shown to contain significant extended warm H_2 emission not explained by heating in PDRs associated with star-formation sites (Cluver et al. 2013). Recently, Appleton et al. (2013) have shown that in Stephan's Quintet [C II] emission is also enhanced in shocked regions and that these regions are coincident with sites of significant kinetic energy dissipation, as evidenced by the existence of large quantities of broad-line (600–700 km s^{-1}), CO-emitting molecular gas. For the turbulent gas between the Taffy galaxies, UGC 12914/5, Peterson et al. (2012) shows similar properties (B. W. Peterson et al. in preparation). Both Stephan's Quintet and the Taffy bridge are intergalactic regions and serve as well-resolved examples of how shocks can heat molecular gas away from other sources of heating. Although perhaps not as extreme as Stephan's Quintet, we find that HCG 57d has exceptional [C II] emission-line properties compared with normal galaxies. HCG 57a shows mildly enhanced [C II] properties and strong star-formation suppression, especially in regions where the velocity field of the molecular gas is highly disturbed. We will discuss the possibility that these galaxies are experiencing boosted molecular and atomic gas heating (over and above that associated with star formation) associated with the recent collision.

4.1. Testing the Validity of PDR Heating for the HCG 57 System

For galaxies in which O+B stars in star-forming regions are the dominant energy source for heating the ISM, the [C II] arises primarily in PDRs associated with diffuse gas heated by photoelectric heating from polycyclic aromatic hydrocarbons and small dust grains (Watson 1972; Draine 1978; Tielens & Hollenbach 1985; Bakes & Tielens 1994). The [C II] emission can also arise from gas collisionally heated by other sources, ranging from hot electrons in an ionized medium (H II regions), shocks or turbulence (Appleton et al. 2013; Lesaffre et al. 2013), to X-ray dissociation regions (XDRs) and cosmic rays. In this case, XDRs are unlikely because the X-ray flux reported for the HCG 57 system in Cluver et al. (2013) was insufficient to power the warm H_2, and they are likely not the dominant heating source of the [C II] either.

Comparing the total luminosities in each line, we see that the [C II]/[O I] ratio is 0.23 for HCG 57d, which is on the extreme lower end of the distribution for the integrated properties of normal galaxies (Malhotra et al. 2001). Figure 9 shows the [C II]/[O I] ratio of HCG 57d as well as the lower limits of the ratio for Regions 1–3 in HCG 57a, compared with their far-IR

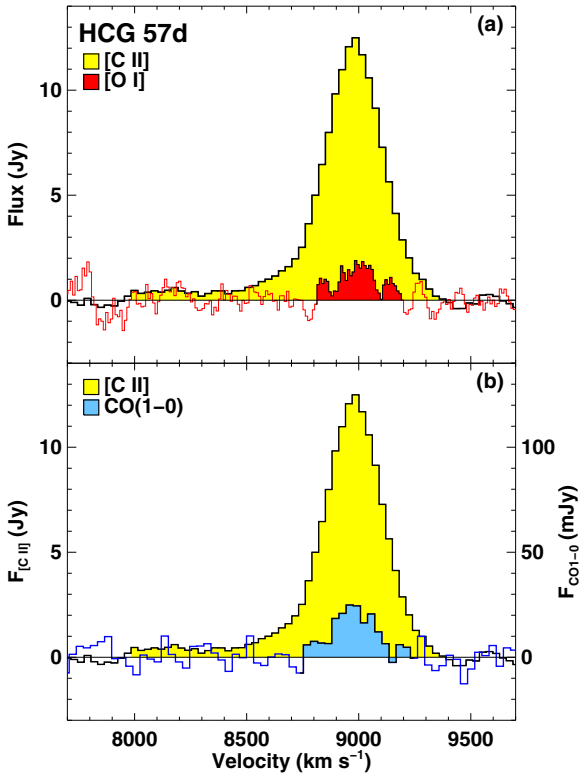

Figure 7. Top: *Herschel* [C II] emission in HCG 57d (yellow) compared to the [O I] emission (red). Both [C II] and [O I] are detected in HCG 57d. The ratio (Table 2) of the integrated [C II] to [O I] line fluxes is on the high end of the distribution for normal galaxies (see text). Bottom: the [C II] spectrum of HCG 57d is compared to the CO(1–0). Again, the integrated flux ratio of CO to [C II] is unusually low compared with normal galaxies.

(A color version of this figure is available in the online journal.)

line cooling, against PDR models of Kaufman et al. (1999), and the starburst ring and diffuse bar regions (extranuclear region S) of NGC 1097 from Beirão et al. (2012). We also show the data for normal galaxies from (Malhotra et al. 2001). The points associated with HCG 57d and the three HCG 57a regions lie in the upper right-hand corner of the available PDR model parameter space. Region 2, which includes the most kinematically disturbed gas, is the most extreme of the HCG 57a individual regions plotted. These points would move farther upward if [O I] had been detected. Based on these IR-line diagnostics alone, the PDR models would require low-UV radiation fields (low G_0) and low densities ($n_{\rm H} < 10^2$ cm^{-3}) and low average gas pressure ($P_{\rm gas} < 10^4$ K cm^{-3}). For reference, we also show the locus of observations from an almost pure extragalactic shock from the Stephan's Quintet filament of Appleton et al. (2013) as a purple box in Figure 9. A mix of shocks combined with higher-density PDRs could therefore also explain the positions of these points on the figure.

Several of the points from the southern diffuse bar region of NGC 1097 (Beirão et al. 2012) occupy regions similar to HCG 57a in Figure 9. These regions of NGC 1097 have long been associated with a strong radio continuum "hook" (Ondrechen & van der Hulst 1983), which is believed to correspond to diffuse gas and plasma compressed in a shock wave associated with the stellar bar. More recent observations and models by Beck et al. (2005) strongly support the idea that this region of NGC 1097 is dominated by highly compressed shocked gas associated with a narrow dust lane, which is instrumental in feeding gas toward the inner part of the galaxy and starburst ring. It is likely that the diffuse [C II] emitting gas in NGC 1097s southern region could also be boosted by shock heating of molecular gas passing through the same compression region. Studies imaging CO in the bar region of NGC 1097 could shed light on how similar it is to the HCG 57 system.

Figure 10 plots the [C II]/$L_{\rm FIR}$ against the CO(1–0)/$L_{\rm FIR}$ of both galaxies, compared to normal and high-redshift galaxies (Stacey et al. 2010). We again show, for reference, the PDR models of Kaufman et al. (1999), but this time including CO emission predictions. The points for both galaxies again lie in the upper far right of the plot, on average beyond the sources in the original Stacey et al. (2010) work. The plot shows that HCG 57d lies significantly above the locus of points for normal galaxies presented by Stacey et al. (2010) and above the "maximum" PDR limit. HCG 57d is outside the extreme edge of a pure PDR model in Figure 10, despite being within the extreme range of PDR models in Figure 9. The host galaxy properties show emission consistent with that of a low-density and low-G_0 PDR ($G_0 < 10^2$), but it would likely require a boost from an additional collisional energy source, either shocks, ionized gas, or a warm neutral (H I) medium to push it above the PDR limit.

For HCG 57a, the [O I], [C II] and CO(1–0) shown in Figures 9 and 10 are in direct disagreement if we assume that photoelectric heating from PDRs is the dominant heat source in both the cold and warm molecular gas. The lower limit to the [C II]/[O I] ratio from Figure 9 indicates that HCG 57a requires a diffuse gas ($n \lesssim 10^3$ cm^{-3}) and low incident G_0. The CO(1–0) and [C II] also require low G_0, though a density one to two orders of magnitude higher is needed to explain the line ratios. The disagreement between the models that fit the [C II], [O I], and CO(1–0) suggests a more complex picture for the ISM in HCG 57a. In fact, HCG 57a may consist of two ISM components, a PDR-dominated component (the interface between young stars and cold gas) and a warmer diffuse component. We note that Region 2, which is the most extreme in Figures 9 and 10, coincides with the position of the IRS slit from Cluver et al. (2013) and likely traces the same emitting area. In this region, L([C II]) $\sim$ L(H_2, warm), consistent with what would be predicted in diffuse shocked molecular gas (Appleton et al. 2013; Lesaffre et al. 2013). Cluver et al. (2013) indicates that the extended warm H_2 emission in HCG 57a requires an additional heating source, and therefore it is likely that a portion of the [C II] is excited by a similar mechanism. Shocks in the diffuse ISM would naturally explain the strong H_2 emission and possible boosting of [C II].

Is it fair to compare the conditions in HCG 57a and 57d to that of the giant shocked filament in Stephan's Quintet? As Appleton et al. (2013) speculated, the isolation of the shocked gas away from significant star formation allowed the effects of shocks to be explored with only minimal PDR contamination in the Quintet. As Cluver et al. (2013) showed, the HCG galaxies with large warm H_2/PAH ratios also have specific star-formation rates that are an order of magnitude lower than normal galaxies, and therefore we might expect that shocks and turbulence, if present, may have a larger proportional effect than in normal galaxies. We note that the HCG 57 system shares some similarities with the Stephan's Quintet shock: (1) broad CO and [C II] lines, (2) enhanced [C II]/FIR emission, and (3) an overabundance of warm molecular hydrogen inconsistent with photoelectric heating by grains in a UV radiation environment. We therefore think that it is reasonable to consider galaxies like HCG 57a and 57d as candidates for shock-boosted warm interstellar gas.

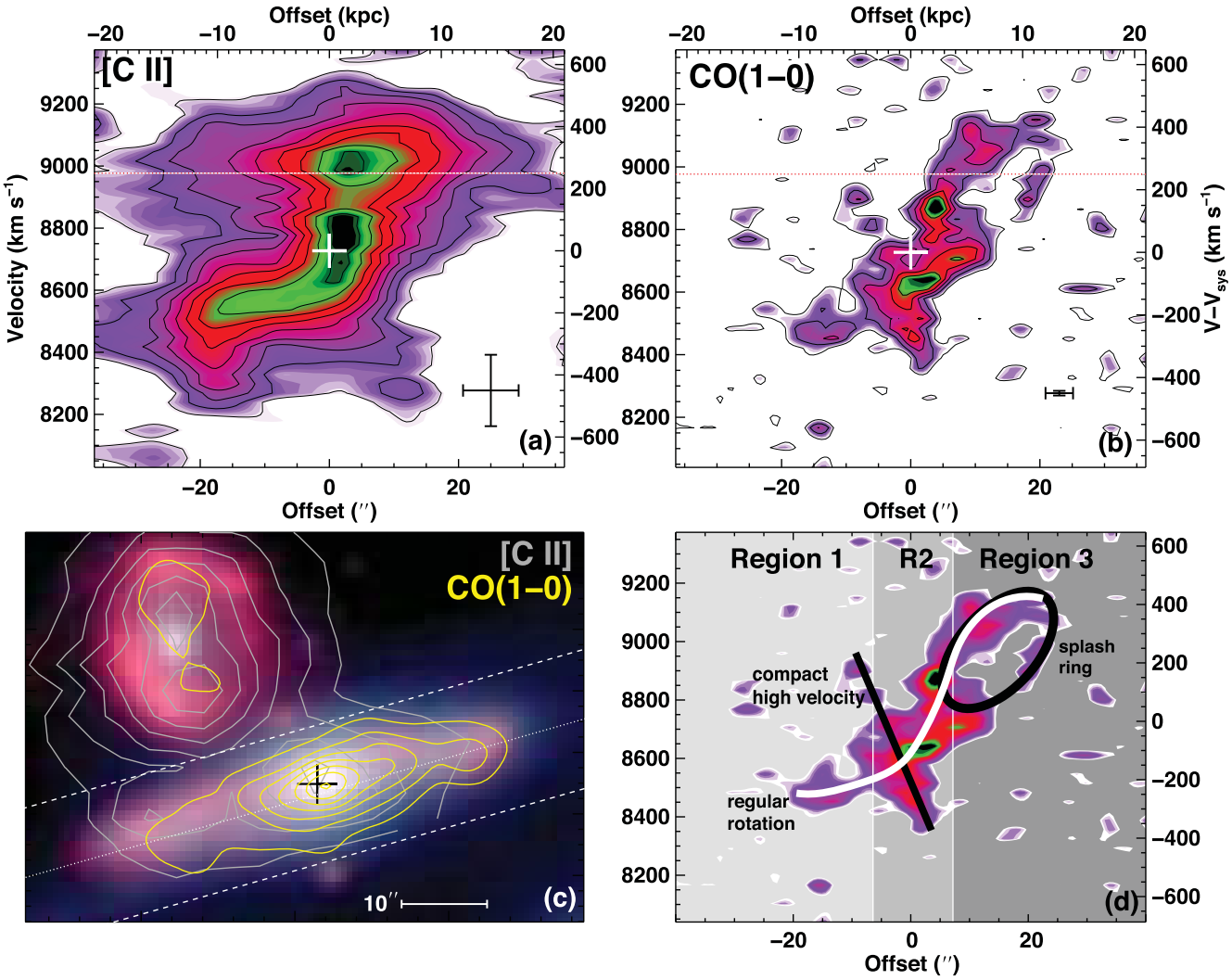

Figure 8. Top left: position–velocity diagram (PVD) in [C II] of HCG 57a. Although it is clear that smoothing of both the pixels and the velocities is an issue, the PVD shows multiple components. There seems to be a [C II] emission component originating at the systemic velocity of HCG 57d, but it is only offset by ≈5″ from the HCG 57a nucleus. Top right: the CO(1–0) PVD, which has been derived from the same spatial box as the [C II], though less extended. The red dotted horizontal line appears in both PVDs and represents the systemic velocity of HCG 57d. The white point represents the velocity and RAcenter of HCG 57a, as determined from a 2MASS K_s-band image. The black points show the uncertainties in each axis. The position of the minimum and maximum velocity offsets for the contours, which for CO(1–0) are −390 and 465 km s^{-1}, and for [C II] are −540 and +580 km s^{-1}. Bottom left: the angle and the boundaries of the region summed (white dashed line), overlaid upon the three-color *Spitzer* IRAC three-color map and the [C II] contours (gray) and CO(1–0) contours (yellow). Bottom right: the CO(1–0) PVD overlaid with a schematic representing the compact high-velocity component (black), the splash ring (black), and regular rotation (white), as well as providing the positions of each region seen in Figure 5, indicating the dominant molecular kinematic components represented in each.

(A color version of this figure is available in the online journal.)

4.2. Can We Rule Out Diffuse Ionized Gas as an Extra Source of [C II] Emission in HCG 57?

To evaluate the importance of diffuse ionized gas from H II regions, we searched for the presence of strong nebular lines, like the [N II] 205 μm line (Beirão et al. 2012) via the deep *Herschel* Spectral and Photometric Imagine Receiver (SPIRE) Fourier Transform Spectrograph (FTS; Griffin et al. 2010) observations. The [N II] 205 μm line is an excellent tracer of ionized gas because its ionization potential lies just above that of neutral hydrogen. The 3σ upper limit for the [N II] 205 μm line in HCG 57a is $<4.5 \times 10^{-18}$ W m^{-2} over the central beam (FWHM = 16.″9 at ν = 1.410 THz) in a pointing centered on Region 2. Scaling up the [C II] for Region 2 by a factor of 1.3 to correct for the larger SPIRE beam, we estimate the [C II]/[N II] 205 μm ratio to be >17. This ratio is at least a factor of 3 to 5 × larger than that associated with H II regions for a reasonable range of densities, and thus we conclude that in the center of HCG 57a the ionized gas contribution to the [C II] emission is small. The SPIRE FTS footprint did not include HCG 57d; therefore, we cannot rule out a contribution to the [C II] emission from H II regions in that galaxy.

Gas with low metallicity can also lead to large values of the [C II]/CO(1-0) ratio through an extended PDR, and this is often found in dwarf systems (e.g., Israel & Maloney 2011). In order to determine whether the [C II]/CO(1–0) ratio was due to such low-metallicity effects, we used the spectrum taken of HCG 57d by the Sloan Digital Sky Survey. Using Equation (11) from Kewley & Dopita (2002), log(O/H)+12 for HCG 57d = 8.648, which is close to solar abundance (HCG 57a does not have an SDSS spectrum available). The fact that the metallicity is so close to solar means that it is unlikely that the [C II]/$L_{\rm FIR}$ ratio is discrepant due to low-metallicity effects. Although the optical fiber of HCG 57d only covers the central 3″ of the galaxy,

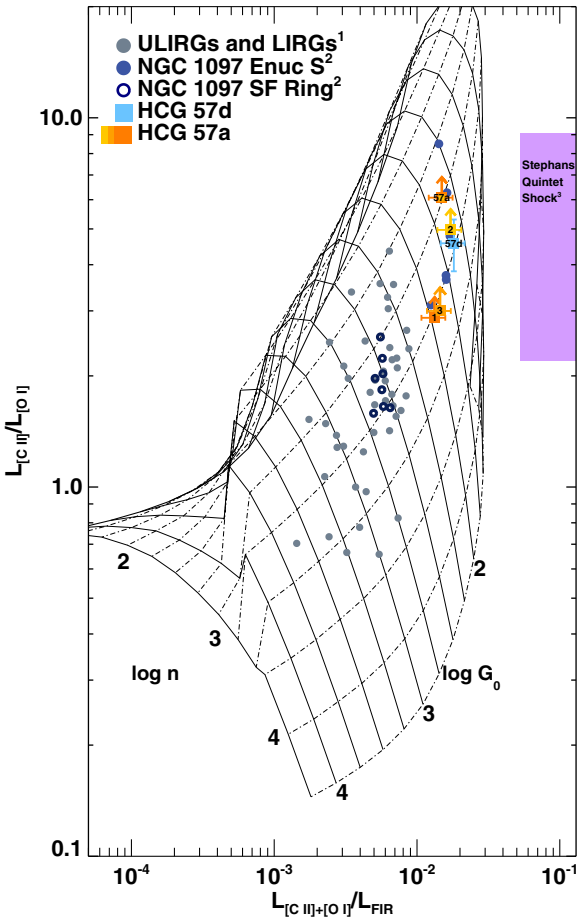

Figure 9. [C II]–to–[O I] ratios plotted against the [C II] and [O I] cooling compared to the far-infrared luminosity, overplotted on PDR models as well as data points from star-forming galaxies from 1: Malhotra et al. (2001) and the resolved *Herschel* data of NGC 1097 from 2: Beirão et al. (2012). Error bars include [C II] and [O I] calibration uncertainties. Extrapolating the expected density n and incident radiation field G_0 indicates that if PDRs are the dominant [O I] and [C II] excitation source for the HCG 57 system, then HCG 57a should be primarily low density and low G_0 with the emission in HCG 57d coming from a slightly higher density gas. It is of note that the lowest density is expected in Region 2, with $n \approx 10^2$ particles per cm^3. The range of [O I] and [C II] emission properties of the Stephan's Quintet shock is shown as a purple box (2: Appleton et al. 2013).

(A color version of this figure is available in the online journal.)

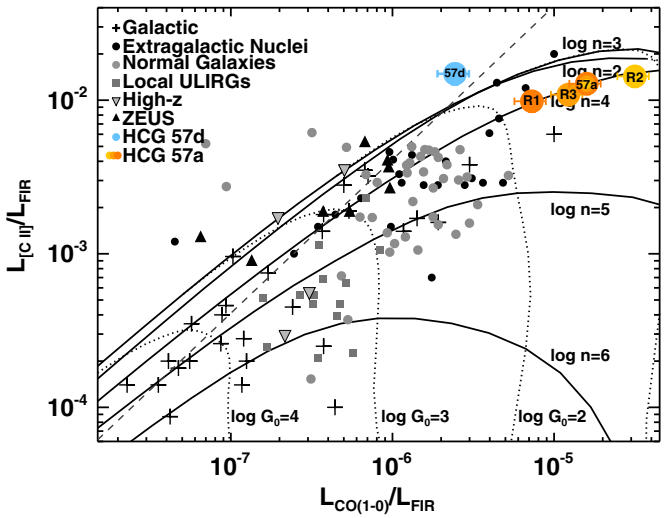

Figure 10. [C II] and CO(1–0) emission measurements of HCG 57 are plotted on the plot originally published in Stacey et al. (2010). Overplotted are the PDR model values as a function of n and G_0 from PDRT (Kaufman et al. 1999). Error bars represent the flux calibration uncertainties of *Herschel* and CARMA. The [C II]/$L_{\rm FIR}$ ratio of HCG 57d is too high to be associated with PDRs. In fact, the $L_{\rm [C\,II]}/L_{\rm CO(1-0)}$ ratio exceeds the theoretical maximum (of 4100; dashed black line) by a factor of ≈1.5. This is an indication that a mechanism other than star formation is partially powering the [C II] emission in the galaxy. If HCG 57a indeed has [C II] emission excited by shocks, then the region points due purely to PDRs would move down from the extremely diffuse gas and the low G_0 to parameters more physical for the amount of CO(1–0) detected by CARMA.

(A color version of this figure is available in the online journal.)

Table 3
HCG 57 CO(1–0) Fluxes, $\Sigma_{\rm H_2}$, and $\Sigma_{\rm SFR}$

Name	$S_{\rm CO}$ (Jy km s^{-1})	$M({\rm H_2})$[a] $\times 10^9$ ($M_\odot$)	log $\Sigma_{\rm mol}$ ($M_\odot$ pc^{-2})	log $\Sigma_{\rm SFR}$ ($M_\odot$ yr^{-1} kpc^{-2})
HCG 57d	5.24[b] ± 1.1	0.78 ± 0.16	0.94	−2.15
HCG 57a	48.6 ± 2.4	7.22 ± 0.35	1.54	−2.53
Region 1	8.93 ± 1.2	1.33 ± 0.18	1.25	−2.54
Region 2	26.9 ± 1.1	3.99 ± 0.16	1.73	−2.44
Region 3	12.0 ± 0.84	1.78 ± 0.13	1.48	−2.67

Notes.
[a] Cold H_2 mass as measured by CO(1–0) and converted using $X_{\rm CO} = 2 \times 10^{20}$ cm^{-2} (K km s^{-1})$^{-1}$ (Bolatto et al. 2013).
[b] Lisenfeld et al. (2014) recovered 10.2 ± 2.1 Jy km s^{-1} in HCG 57d, corresponding to a total molecular mass of 2.28 ± 0.47 × 10^9 $M_\odot$.

it is unlikely that such a small galaxy could experience a strong metallicity gradient. Deep optical integral field spectroscopy of ionized gas in HCG 57d may further illuminate the reason for the boosted [C II]/$L_{\rm FIR}$, by providing spatially resolved ionized gas ratios, which are able to determine the dominant source of ionization (Kewley et al. 2006).

4.3. Suppressed Star Formation in HCG 57a?

The molecular gas mass and surface densities of HCG 57a and HCG 57d were calculated based on the CO(1–0) map, convolved to a point-spread function of 9.″4 and registered to the [C II] map, which was chosen to allow the regions to remain consistent throughout this paper. The mass of H_2 for a given flux was determined assuming the standard $L_{\rm CO}$-to-M(H_2) conversion factor of (Bolatto et al. 2013):

$$\frac{M(H_2)}{M_\odot} = 8.47 \times 10^3 \left(\frac{D}{\rm Mpc}\right)^2 \left(\frac{\int S_\nu \Delta v}{\rm Jy\,km\,s^{-1}}\right).$$

The total H_2 masses calculated for HCG 57a and 57d are listed in Table 3,[23] of 7.22 × 10^9 $M_\odot$ for HCG 57a and 2.28 × 10^9 $M_\odot$ for HCG 57d. The stellar masses calculated in Bitsakis et al. (2014) of 2.0 × 10^{11} $M_\odot$ and 2.5 × 10^{10} $M_\odot$ for HCG 57a and 57d, respectively, correspond to molecular gas-to-stellar mass fractions of 3.6% and 9.1%, respectively, which is in the normal range for late-type galaxies. The lower limit to the molecular fraction[24] on the other hand is quite high. The total group H I mass from Verdes-Montenegro et al. (2001) is 5.1 × 10^9 $M_\odot$. The HCG 57 group is composed of two subgroups (Figure 11), and therefore the H I mass listed is an upper limit to the HCG 57a, c, d complex within the group. Including $M(H_2)$ contributions from HCG 57a and 57d only, we derive the lower limit to the molecular fraction of $f_{\rm mol} > 0.65$ for the entire HCG 57 group, which is likely more dominant if the H I is distributed

[23] We use the total H_2 mass from Lisenfeld et al. (2014) for HCG 57d in the following analysis.
[24] Molecular-to-neutral gas fraction.

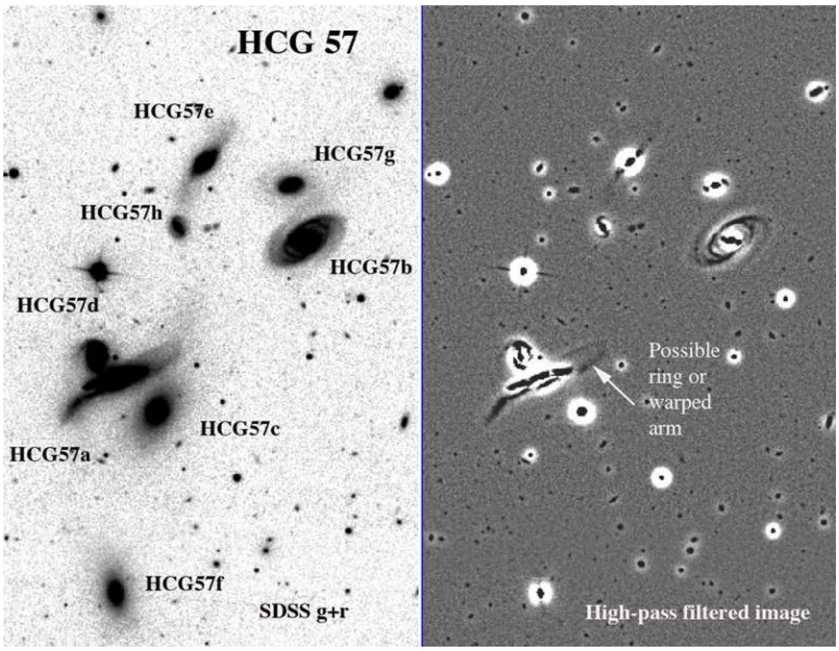

Figure 11. Left: the SDSS g and r images summed to bring out faint structure for the HCG 57 group. Our paper concentrates on the HCG 57a,d subsystem. Right: A high-pass filtered version of the same image after subtracting the image from a smoothed version of itself (smoothed with a Gaussian with a $\sigma = 3$ pixels), which suppresses extended structure and emphasizes sharp features in the image, such as the spiral arms in HCG 57b, nuclear bar structures, and the ring/ring-arcs in HCG 57a and d).

more uniformly across the group (which is likely). A larger survey along the sequence of compact group H I depletion (Verdes-Montenegro et al. 2001) will shed light on whether there is a relationship between the molecular gas fraction and H I starvation (K. Alatalo et al. 2014, in preparation).

The gas surface density Σ_{H_2} was then determined by dividing by the area in which CO(1–0) was detected, based on the areas shown in Figure 5. The *GALEX* far-ultraviolet broadband and the *Spitzer* 24 μm maps were sky-subtracted using the IDL routine `sky`[25] from the NASA Goddard IDL Astronomy User's Library, then convolved to 9.″4 and registered to the [C II] map as well, to allow matching resolution and matching pixels for all maps used to determine the SF rate and gas surface density. The SF rate was then determined from the FUV+24 μm conversion from Leroy et al. (2008), normalized to a Salpeter Initial Mass Function (Salpeter 1955; for comparison to the original Kennicutt 1998 sample). The SFRs of HCG 57a and 57d estimated from this method agreed well with the SFRs derived in Bitsakis et al. (2014). The SFR was averaged over the same pixels that had nonzero emission in the CO(1–0) moment-0 map within each of the pertinent regions. The CO fluxes, H_2 masses, and surface densities are listed in Table 3.

Figure 12 shows the Kennicutt–Schmidt relation (K-S; Kennicutt 1998) of HCG 57d and the three regions of HCG 57a compared to other objects, including the Milky Way (Yusef-Zadeh et al. 2009), normal galaxies (Kennicutt 1998; Fisher et al. 2013), high-redshift objects (Genzel et al. 2010), and radio galaxies (Ogle et al. 2010). While HCG 57d appears to agree with the relation, HCG 57a appears to be suppressed by a factor of 5–18. In fact, the observed suppression seems to correlate with regions of the CO(1–0) PVD with multiple kinematic components along the line of sight (Figure 8(b)). The R1, which sits nearest to the K-S relation, only contains one kinematic component, belonging to the rotating disk. On the other hand,

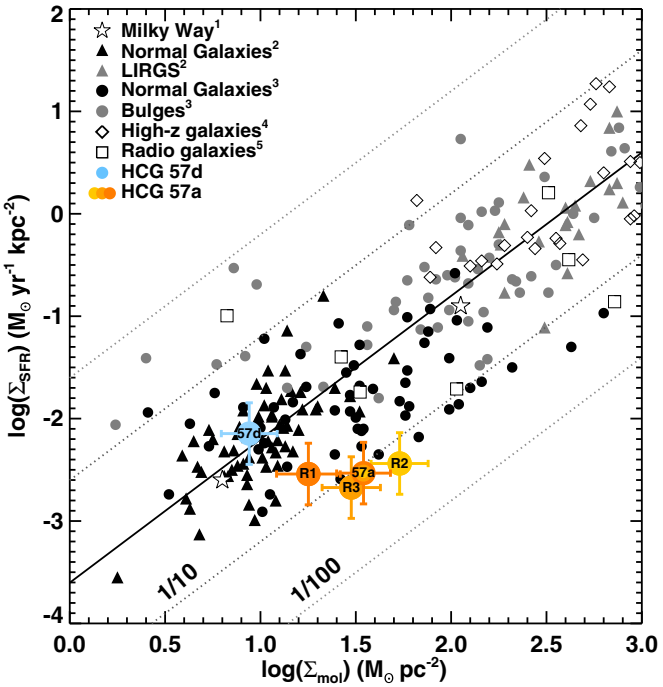

Figure 12. Star formation and gas density within the HCG 57 system (derived in Section 3) are shown in comparison to their position on the Kennicutt–Schmidt relation (Kennicutt 1998), including HCG 57d, the integrated HCG 57a point, as well as the regions. The SFR was calculated using the 24 μm *Spitzer* data combined with the far-UV data from *GALEX*, using Leroy et al. (2008), normalized to a Salpeter initial mass function (IMF). Error bars represent the scatter in the 24 μm-to-SFR conversion (Calzetti et al. 2007) and the calibration uncertainties and L_{CO}-to-H_2 conversion. HCG 57d and regions of HCG 57a are compared to SF-to-gas density for objects including the Milky Way (1: Yusef-Zadeh et al. 2009), normal galaxies and bulges (2: Kennicutt 1998, 3: Fisher et al. 2013), high-redshift objects (4: Genzel et al. 2010), and radio galaxies (5: Ogle et al. 2010; Alatalo et al. 2014), all renormalized to a Salpeter IMF. The lines shown represent the Kennicutt–Schmidt relation and the 1/10 and 1/100 suppression and enhancement lines.

(A color version of this figure is available in the online journal.)

[25] http://idlastro.gsfc.nasa.gov/ftp/pro/idlphot/sky.pro

both R2 and R3 contain multiple kinematic components (the regular rotation, compact high velocity, and splash-ring components) along the line of sight are also the objects that appear the farthest from the K-S relation.

The fact that the suppressed regions of the galaxy correspond quite well to the regions with disturbed kinematics in the PVD points to the possibility that the interaction that caused the large velocity disturbances seen in the galaxy are also currently suppressing the SF in those regions. The CO kinematics in HCG 57d and R1 are both regular, predicting that those regions would form stars normally, and, indeed, it appears that they do. In contrast, R2 and R3 have CO kinematics that do not indicate simple rotation alone. Star formation requires fragmentation of the gaseous disk because of gravitational instabilities. If another source of heating was available to the gas (such as turbulence), it could be changing the balance between kinetic energy and potential energy and therefore reducing the efficiency of SF. The large amount of rotationally excited H_2 seen in HCG 57a (Cluver et al. 2013), as well as the high[C II]/FIR and [C II]/CO(1–0) ratios, points to the likelihood that an additional heating source operates in this galaxy, perhaps turbulence and shocks.

Guillard et al. (2012a) argued in the context of Stephan's Quintet that a shock is able to inject turbulent energy and heat the molecular gas in the system, stabilizing it against collapse, and thus explain why we see such a low SFR in the most kinematically disturbed regions of HCG 57a. If the [C II] enhancement and CO(1–0) kinematics are indeed due to shock dynamics, this is a natural explanation for the suppression of SF seen in HCG 57a.

On the other hand, the fact that the molecular gas that falls the farthest from the K-S relation tends to be the most kinematically disturbed is suggestive of another possibility for the suppression, namely, assuming that a particular L(CO)–M(H_2) relationship holds for most external systems, when the relation has been measured and constrained using virialized giant molecular clouds within the Milky Way (Solomon et al. 1987). If the underlying clouds in the kinematically disturbed portions of HCG 57a have a smoother distribution, as is seen in ultraluminous infrared galaxies (ULIRGS; Downes & Solomon 1998), then X_{CO} could be a factor of ≈2–3 lower (Sandstrom et al. 2013). Bitsakis et al. (2014) calculated the gas-to-dust ratios in the HCG 57 system and found the dust mass in HCG 57d to be $7.8 \times 10^6\ M_\odot$ and HCG 57a to be $4.0 \times 10^7\ M_\odot$. If HCG 57a and 57d have a standard gas-to-dust ratio of ≈150, consistent with that found in a large sample of HCGs (K. Alatalo et al. 2014, in preparation) as well as with the Taffy Galaxies (Zhu et al. 2007), then the gas mass derived using the Bolatto et al. (2013) X_{CO} conversion is consistent within errors.

4.4. Deciphering the Interaction History of HCG 57a and 57d

The enhanced [C II] emission, disturbed CO(1–0) kinematics, and suppressed SF in the HCG 57 system point to an interesting recent interaction history between HCG 57a and HCG 57d. We show in Figure 11 an SDSS view of the HCG 57 group as a whole (left = sum of SDSS g and r images and right = same image after application of a high-pass filter to bring out the narrow structures). It is clear from the images that HCG 57a and d show signs of interaction, and both systems contain complete or partial ring-like structures. Although we cannot rule out recent interaction with other group members, the most likely cause of the warped nature of HCG 57a is its nearby companion HCG 57d.

We hypothesize that HCG 57d, the smaller companion, has recently splashed through HCG 57a, but it did so off-center, creating a collisional ring (Appleton & Struck-Marcell 2006) in HCG 57d and inducing a strong ring disturbance in the edge-on galaxy HCG 57a. The offset between the center of the ring and the nucleus is 2 arcsec (0.3× the minor axis radius of the ring) as measured on the SDSS g image. This is similar to, for example, the offset in the famous offset ring the "Cartwheel" and Arp 10 (Appleton & Marston 1997; Charmandaris, Appleton & Marston 1993). Models of off-center collisions (e.g., Toomre 1978, Figure 5; Appleton & Struck-Marcell 1987; and Gerber & Lamb 1994) show that this kind of offset is created when the impact parameter between the two galaxies is roughly 1/4 of the radius of the disk.

This off-center collision hypothesis is also able to explain why the SDSS and *Spitzer* images from Figures 1 and 2 show the nucleus of the smaller galaxy to be offset from the center of its star-forming ring, a common prediction for nonzero impact parameter ring galaxies (Appleton & Struck-Marcell 2006). In this picture, both galaxies should evolve into galaxies with rings or ring segments, depending how offset the collision is. The partial ring or warped arm seen in the high-pass filtered image of HCG 57a could be interpreted as such a collisionally driven ring wave that is also warped by the passage of HCG 57d through the disk of HCG 57a.

Although the above scenario is speculative, it might explain the peculiar kinematics of HCG 57a seen in the CARMA data, especially the upper right-hand corner of the PVD (Figure 8), where the double line profiles could be interpreted as being part of a radially expanding wave centered to the northwest of the galaxy's center. The characteristic timescale of the high-velocity PVD feature on the northwestern side of HCG 57a is about 50 Myr (assuming an expansion velocity of $100\ \mathrm{km\ s^{-1}}$ and a radius of 5 kpc), which is shorter than the approximate rotational timescale of the galaxy of approximately 160 Myr, implying that if this is the kinematic signature of an expanding wave, it has not fully disturbed the whole disk. Without a detailed model of the gas and stellar dynamics of a collision, it is hard to further quantify. Given that this is a quite dense association of galaxies, we cannot rule out other members of the group having also played a role.

Even without a proper model of the proposed collision between HCG 57a and d, it is interesting to note that the most SF-suppressed regions of HCG 57a (Regions 2 and 3 in Figure 12) are also the regions with the largest velocity disturbances (Figure 8(b)). This is consistent with the results seen in Stephan's Quintet filament, where multiple broad CO velocity components, symptomatic of kinetic energy dissipation in the molecular gas, are found to be associated with low star-formation rates (Guillard et al. 2012a; Konstantopoulos et al. 2014). It is possible therefore that strong kinematic disturbances, caused by galaxy collisions, can suppress star formation.

We finally come to the question of why HCG 57a and d have such different [C II]/CO ratios. Our observations have shown that HCG 57d has received a boost in its [C II] emission relative to that expected from PDR models and that HCG 57a could potentially also be enhanced, but to a lesser degree. One reason may have to do with the relative stellar masses of the two galaxies (of $2.0 \times 10^{11}\ M_\odot$ for HCG 57a and $2.5 \times 10^{10}\ M_\odot$ for HCG 57d; Bitsakis et al. 2014). High values of [C II] to CO ratios are not uncommon in low-metallicity dwarf systems (Poglitsch et al. 1995; Stacey et al. 1991; Israel et al. 1996; Israel & Maloney 2011; Madden et al. 1997), and in such systems

the "dark gas" fraction (i.e., molecular gas not traced by CO) is expected to increase with lower metallicity (Wolfire et al. 2010). However, we believe that HCG 57d is closer to solar oxygen metallicity (see earlier), and thus the dark molecular fraction is likely to be modest.

Instead, we suggest that the collision between the two galaxies could create an enhancement in the diffuse component relative to the denser molecular gas by a different mechanism. HCG 57d, being the smaller of the two galaxies, would receive a significantly stronger perturbation than HCG 57a, and this would inject more kinetic energy into the ISM of that galaxy, as well as causing almost all of the gas in the galaxy to be affected quickly because of its small size. Furthermore, if the galaxy has indeed crashed through the disk of HCG 57a, the diffuse gas in the galaxy would be significantly affected and heated. Although we do not have sufficient spatial resolution in the Herschel observations to determine whether the [C II] emission is much more extended than the denser molecular gas, one plausible explanation for the enhanced [C II] emission is that the collision excited a much larger volume of diffuse gas than the denser CO molecular gas, thus increasing the observed ratio.

4.5. The HCG 57 System in Context

The gas-on-gas collision that HCG 57 has recently experienced is a common occurrence in Hickson compact groups (Hickson 1997) because of their high space densities and low galaxy velocity dispersions. This environment predisposes galaxies to interact with one another and is likely a conduit for rapid evolution, as suggested by the dearth of galaxies in the infrared (IR) green valley (Johnson et al. 2007; Cluver et al. 2013). The MOHEG systems in particular seem to be in a special portion of their evolution, as these galaxies tend to be the ones found in the IR green valley (Cluver et al. 2013), rapidly transitioning from blue and star-forming to red and dead.

The suppressed SF seen in HCG 57a might be a beacon pointing toward the physics that dictates how that transition takes place. The scenario we put forward is that when two galaxies within the compact group have a direct collision, the gas is heated through shocks, suppressing star formation in the immediate term because of the injection of the extra kinetic energy to the molecular gas via turbulence (Guillard et al. 2009, 2012a; Appleton et al. 2013). Shocks in general are shown to enhance SF (Jog & Solomon 1992; Barnes & Hernquist 1996; Elmegreen & Efremov 1997), but we hypothesize that this SF enhancement requires a sufficient amount of time for the cooling lines to efficiently shed the energy that was injected by turbulence, which is effectively balanced by gravity. Once the turbulence has been efficiently cooled, the larger density of the postshock gas determines the SF enhancement. It is likely that the suppression that is seen in HCG 57a is transient, but this speaks to the role that turbulence likely plays in inhibiting SF. On longer scales, HCGs will also suffer from harassment (Icke 1985; Mihos 1995; Moore et al. 1996; Bekki 1998) and ram pressure stripping (Cayatte et al. 1990; Böhringer et al. 1994, although this was argued against in Cluver et al. 2013), and these can remove the ISM, effectively shutting down future SF and transitioning the galaxy.

High-redshift galaxies are known to contain more turbulent gas (Shapiro et al. 2009), and therefore it is important to understand to what degree turbulence modifies SF, both by enhancing it and suppressing it. Studying MOHEGs within HCGs is an ideal way to gauge the role of turbulence in environments already known to be extreme, and the HCG 57 system has shown itself to be an ideal test case.

5. SUMMARY

We presented the [O I], [C II], and CO(1–0) maps taken using the *Herschel Space Observatory* and the CARMA array of the Hickson compact group galaxies HCG 57a and HCG 57d, in which HCG 57a is a known MOHEG.

1. The [C II]/$L_{\rm FIR}$ ratio in HCG 57d is too large to be explained with photoelectric heating in PDRs alone. Two possible explanations for the boosted [C II]/$L_{\rm FIR}$ are copious amounts of ionized gas and possibly the shock excitation of a larger volume of diffuse gas compared with the denser molecular gas resulting from HCG 57d having crashed through the disk of HCG 57a. Excitation of [C II] by neutral gas is unlikely because of the low observed H I content of the HCG 57 group.
2. The [C II]/CO(1–0) ratio of HCG 57a is also more easily explained if one assumes that a shock has traversed the system, boosting the [C II] emission and resolving discrepancies in the PDR models needed to explain the CO(1–0)/$L_{\rm FIR}$ and [C II]/$L_{\rm FIR}$ ratios. The SPIRE FTS upper limits to the detection of the [N II] 205 μm line allow us to rule out copious ionized gas as the boosting agent in this case. The approximate equality in the cooling power of warm H_2 mid-IR emission and [C II] emission, detected in the center of HCG 57a, is consistent with models of shocks or turbulence boosting the [C II] emission relative to PDR emission.
3. The CO(1–0) gas kinematics in HCG 57a show a complex structure, including regions with kinematic components beyond the simple galactic rotation curve. The star formation is suppressed preferentially in those regions with complex kinematic structures, by factors of 30–40 (as compared with normal efficiencies in HCG 57d and R1, both of which have simple molecular gas kinematics). The dust-to-gas ratio in HCG 57a appears to be consistent with that seen in other HCGs using a "standard" $L_{\rm CO}$–M(H_2) conversion factor, and we hypothesize that the current suppression has been brought on by injected turbulence.
4. A collision between HCG 57a and HCG 57d 50 Myr ago, where HCG 57d directly intersected the disk of HCG 57a, would possibly explain both the unusual [C II] properties and the star formation suppression. In HCG 57d, the collisionally induced shock has already traversed the entire disk of the galaxy, and [C II] cooling has been enhanced, allowing for efficient star formation in the (now denser) postshock gas. The shock, on the other hand, has not completely traversed HCG 57a, meaning that turbulent injection is still taking place in the disk. This extra energy injection counteracts efficient fragmentation and gravitational collapse, therefore suppressing star formation. These processes may cause rapid termination of star formation, leading to rapid evolution of the galaxy through the mid-infrared green valley.

K.A. thanks Drew Brisbin and Gordon Stacey for giving access to the data and code used to create the [C II]/CO comparison figure used in this paper and the anonymous referee for insightful recommendations that have improved the paper. K.A. and P.N.A. are supported by funding through *Herschel*, a European Space Agency Cornerstone Mission with significant participation by

NASA, through an award issued by JPL/Caltech. U.L. acknowledges support by the research projects AYA2011-24728 from the Spanish Ministerio de Ciencia y Educación and the Junta de Andalucía (Spain) grants FQM108. T.B. and V.C. acknowledge partial support from the EU FP7 grant PIRSES-GA-2012-316788. The work of L.V.M. has been supported by grant AYA2011-30491-C02-01 cofinanced by MICINN and FEDER funds, and the Junta de Andalucía (Spain) grants P08-FQM-4205 and TIC-114. Support for CARMA construction was derived from the Gordon and Betty Moore Foundation, the Kenneth T. and Eileen L. Norris Foundation, the James S. McDonnell Foundation, the Associates of the California Institute of Technology, the University of Chicago, the states of California, Illinois, and Maryland, and the National Science Foundation. Ongoing CARMA development and operations are supported by the National Science Foundation under a cooperative agreement and by the CARMA partner universities. *Herschel* is an ESA space observatory with science instruments provided by European-led Principal Investigator consortia and with important participation from NASA. This work is based (in part) on observations made with the *Spitzer Space Telescope*, which is operated by the Jet Propulsion Laboratory, California Institute of Technology under a contract with NASA. Funding for the SDSS and SDSS-II has been provided by the Alfred P. Sloan Foundation, the Participating Institutions, the National Science Foundation, the U.S. Department of Energy, the National Aeronautics and Space Administration, the Japanese Monbukagakusho, the Max Planck Society, and the Higher Education Funding Council for England. The SDSS Web Site is http://www.sdss.org/.

REFERENCES

Alatalo, K., Davis, T. A., Bureau, M., et al. 2013, MNRAS, 432, 1796
Alatalo, K., Lacy, M., Lanz, L., et al. 2014, ApJ, submitted (arXiv:1410.4556)
Appleton, P. N., Guillard, P., Boulanger, F., et al. 2013, ApJ, 777, 66
Appleton, P. N., & Marston, A. P. 1997, AJ, 113, 201
Appleton, P. N., & Struck-Marcell, C. 1987, ApJ, 318, 103
Appleton, P. N., & Struck-Marcell, C. 2006, FCPh, 16, 111
Appleton, P. N., Xu, K. C., Reach, W., et al. 2006, ApJL, 639, L51
Bakes, E. L. O., & Tielens, A. G. G. M. 1994, ApJ, 427, 822
Barnes, J. E., & Hernquist, L. 1996, ApJ, 471, 11
Beck, R., Fletcher, A., Shukurov, A., et al. 2005, A&A, 444, 739
Beirão, P., Armus, L., Helou, G., et al. 2012, ApJ, 751, 144
Bekki, K. 1998, ApJL, 502, L133
Bitsakis, T., Charmandaris, V., Appleton, P. N., et al. 2014, A&A, 565, 25
Bitsakis, T., Charmandaris, V., da Cunha, E., et al. 2011, A&A, 533, 142
Bitsakis, T., Charmandaris, V., Le Floc'h, E., et al. 2010, A&A, 517, 75
Bolatto, A. D., Wolfire, M., & Leroy, A. K. 2013, ARA&A, 51, 207
Böhringer, H., Briel, U. G., Schwarz, R. A., et al. 1994, Natur, 368, 828
Borthakur, S., Yun, M., & Verdes-Montenegro, L. 2010, ApJ, 710, 385
Bournaud, F., Chapon, D., Teyssier, R., et al. 2011, ApJ, 730, 4
Cayatte, V., van Gorkom, J. H., Balkowski, C., & Kotanyi, C. 1990, AJ, 100, 604
Calzetti, D., Kennicutt, R. C., Engelbracht, C. W., et al. 2007, ApJ, 666, 870
Charmandaris, V., Appleton, P. N., & Marston, A. P. 1993, ApJ, 414, 154
Cluver, M. E., Appleton, P. N., Boulanger, F., et al. 2010, ApJ, 710, 248
Cluver, M. E., Appleton, P. N., Ogle, P., et al. 2013, ApJ, 765, 93
de Looze, I., Baes, M., Bendo, G. J., Cortese, L., & Fritz, J. 2011, MNRAS, 416, 2712
Downes, D., & Solomon, P. M. 1998, ApJ, 507, 615
Draine, B. T. 1978, ApJS, 36, 595
Elmegreen, B. G., & Efremov, Y. N. 1997, ApJ, 480, 235
Fisher, D. B., Bolatto, A., Drory, N., et al. 2013, ApJ, 764, 174
Genzel, R., Tacconi, L. J., Gracia-Carpio, J., et al. 2010, MNRAS, 407, 2091
Gerber, R. A., & Lamb, S. A. 1994, ApJ, 431, 604
Griffin, M. J., Abergel, A., Abreu, A., et al. 2010, A&A, 518, L3
Guillard, P., Boulanger, F., Lehnert, M. D., et al. 2014, A&A, submitted
Guillard, P., Boulanger, F., Pineau Des Forêts, G., & Appleton, P. N. 2009, A&A, 502, 515
Guillard, P., Boulanger, F., Pineau de Forêts, G., et al. 2012a, ApJ, 749, 158
Guillard, P., Ogle, P. W]M., Emonts, B. C. H., et al. 2012b, ApJ, 747, 95
Helou, G., Khan, I. R., Malek, L., & Boehmer, L. 1998, ApJS, 68, 151
Helou, G., Roussel, H., Appleton, P., et al. 2004, ApJS, 154, 253
Hickson, P. 1982, ApJ, 255, 382
Hickson, P. 1997, ARA&A, 35, 357
Icke, V. 1985, A&A, 144, 115
Israel, F. P., & Maloney, P. R. 2011, A&A, 531, A19
Israel, F. P., Maloney, P. R., Geis, N., et al. 1996, ApJ, 465, 738
Jog, C. J., & Solomon, P. M. 1992, ApJ, 387, 152
Johnson, K. E., Hibbard, J. E., Gallagher, S. C., et al. 2007, AJ, 134, 1522
Kaufman, M. J., Wolfire, M. G., Hollenbach, D. J., & Luhman, M. L. 1999, ApJ, 527, 795
Kennicutt, R. C. 1998, ApJ, 498, 541
Kewley, L. J., & Dopita, M. A. 2002, ApJS, 142, 35
Kewley, L. J., Groves, B., Kauffmann, G., & Heckman, T. 2006, MNRAS, 372, 961
Konstantopoulos, I. S., Appleton, P. N., Guillard, P., et al. 2014, ApJ, 784, 1
Konstantopoulos, I. S., Gallagher, S. C., Fedetov, K., et al. 2010, ApJ, 723, 197
Lacy, M., Storrie-Lombardi, L. J., Sajina, A., et al. 2004, ApJS, 154, 166
Leroy, A. K., Walter, F., Brinks, E., et al. 2008, AJ, 136, 2782
Lesaffre, P., Pineau de Forêts, G., Godard, B., et al. 2013, A&A, 550, 106
Lisenfeld, U., Appleton, P. N., Cluver, M. E., et al. 2014, A&A, 570, 24
Madden, S. C., Poglitsch, A., Geis, N., Stacey, G. J., & Townes, C. H. 1997, ApJ, 483, 200
Malhotra, S., Kaufman, M. J., Hollenbach, D., et al. 2001, ApJ, 561, 766
Martínez, M. A., Del Olmo, A., Coziol, R., & Perea, J. 2010, AJ, 139, 1199
Mihos, J. C. 1995, ApJL, 438, L75
Moore, B., Katz, N., Lake, G., Dressler, A., & Oemler, A. 1996, Natur, 379, 613
Nesvadba, N. P. H., Boulanger, F., Salomé, P., et al. 2010, A&A, 521, 65
Ogle, P. M., Antonucci, R., Appleton, P. N., & Whysong, D. 2007, ApJ, 668, 699
Ogle, P. M., Boulanger, F., Guillard, P., et al. 2010, ApJ, 724, 1193
Ondrechen, M. P., & van der Hulst, J. M. 1983, ApJL, 269, L47
Peterson, B. W., Appleton, P. N., Helou, G., et al. 2012, ApJ, 751, 11
Pilbratt, G. L., Riedinger, J. R., Passvogel, T., et al. 2010, A&A, 518, L1
Poglitsch, A., Krabbe, A., Madden, S. C., et al. 1995, ApJ, 454, 293
Poglitsch, A., Waelkens, C., Geis, N., et al. 2010, A&A, 518, L2
Rasmussen, J., Ponman, T. J., Verdes-Montenegro, L., Yun, M. S., & Borthakur, S. 2008, MNRAS, 388, 1245
Saitoh, T. R., Daisaka, H., Kokubo, E., et al. 2009, PASJ, 61, 481
Salpeter, E. E. 1955, ApJ, 121, 161
Sanders, D. B., & Mirabel, I. F. 1996, ARA&A, 34, 749
Sandstrom, K. M., Leroy, A. K., Walter, F., et al. 2013, ApJ, 777, 5
Sault, R. J., Teuben, P. J., & Wright, M. C. H. 1995, in ASP Conf. Ser. 77, Astronomical Data Analysis Software and Systems IV, ed. R. A. Shaw, H. E. Payne, & J. J. E. Hayes (San Francisco, CA: ASP), 433
Shapiro, K. L., Genzel, R., Quataert, E., et al. 2009, ApJ, 701, 955
Skrutskie, M. F., Cutri, R. M., Stiening, R., et al. 2006, AJ, 131, 1163
Solomon, P. M., Rivolo, A. R., Barrett, J., & Yahil, A. 1987, ApJ, 319, 730
Stacey, G. J., Geis, N., Genzel, R., et al. 1991, ApJ, 373, 423
Stacey, G. J., Hailey-Dunsheath, S., Ferkinoff, C., et al. 2010, ApJ, 724, 957
Teyssier, R., Chapon, D., & Bournaud, F. 2010, ApJL, 720, L49
The Planck Collaboration, Ade, P. A. R., Aghanim, N., et al. 2013, A&A, in press (arXiv:1303.5076)
Tielens, A. G. G. M., & Hollenbach, D. 1985, ApJ, 291, 722
Toomre, A. 1978, IAUC, 79, 109
Torres-Flores, S., Amram, P., Mendes de Oliveira, C., et al. 2014, MNRAS, 442, 2188
Tzanavaris, P., Hornschemeier, A. E., Gallagher, S. C., et al. 2010, ApJ, 716, 556
Verdes-Montenegro, L., Yun, M. S., Williams, B. A., et al. 2001, A&A, 377, 812
Walker, L. M., Butterfield, N., Johnson, K. E., et al. 2013, ApJ, 775, 129
Walker, L. M., Johnson, K. E., Gallagher, S. C., et al. 2010, AJ, 140, 1254
Walker, L. M., Johnson, K. E., Gallagher, S. C., et al. 2012, AJ, 143, 69
Watson, W. D. 1972, ApJ, 176, 103
Wolfire, M. G., Hollenbach, D., & McKee, C. F. 2010, ApJ, 716, 1191
Yusef-Zadeh, F., Hewitt, J. W., Arendt, R. G., et al. 2009, ApJ, 702, 178
Zhu, M., Gao, Y., Seaquist, E. R., & Dunne, L. 2007, AJ, 134, 118